Lawrence Berkeley National Laboratory

Lawrence Berkeley National Laboratory

Title

Parameter estimation from flowing fluid temperature logging data in unsaturated fractured rock using multiphase inverse modeling

Permalink

https://escholarship.org/uc/item/9r57z6g6

Author

Mukhopadhyay, S.

Publication Date

2009-05-21

eScholarship.org Powered by the California Digital Library
University of California

Parameter Estimation From Flowing Fluid Temperature Logging Data In Unsaturated Fractured Rock Using Multiphase Inverse Modeling

Sumit Mukhopadhyay, Yvonne W. Tsang, and Stefan Finsterle
Lawrence Berkeley National Laboratory, Berkeley, CA 94720

Abstract

A simple conceptual model has been recently developed for analyzing pressure and temperature data from flowing fluid temperature logging (FFTL) in unsaturated fractured rock. Using this conceptual model, we developed an analytical solution for FFTL pressure response, and a semi-analytical solution for FFTL temperature response. We also proposed a method for estimating fracture permeability from FFTL temperature data. The conceptual model was based on some simplifying assumptions, particularly a single-phase air flow model was used. In this paper, we develop a more comprehensive numerical model of multiphase flow and heat transfer associated with FFTL. Using this numerical model, we perform a number of forward simulations to determine the parameters that have the strongest influence on the pressure and temperature response from FFTL. We then use the *i*TOUGH2 optimization code to estimate these most sensitive parameters through inverse modeling and to quantify the uncertainties associated with these estimated parameters. We conclude that FFTL can be utilized to determine permeability, porosity, and thermal conductivity of the fracture rock. Two other parameters, which are not properties of the fractured rock, have strong influence on FFTL response. These are pressure and temperature in the borehole that were at equilibrium with the fractured rock formation at the beginning of FFTL. We illustrate how these parameters can also be estimated from FFTL data.

1. Introduction

In a recent paper [*Mukhopadhyay and Tsang*, 2008], hereafter referred to as Paper I, we presented a simple conceptual model and a semi-analytical solution to analyze the data from flowing fluid temperature logging (FFTL). In Paper I, we also presented a procedure to estimate the effective permeability of the fractured rock using the temperature data from FFTL (see Section 2 for a recapitulation of FFTL). The conceptual model described in Paper I assumes single-phase flow of air and ignores the presence of the water phase in the unsaturated rock. The model includes heat transfer by convection but neglects heat conduction. It also assumes that pumping of air from the borehole during FFTL does not change the pressure and temperature in the surrounding rock (a reasonable assumption, considering the short duration of the test and the large volume of the surrounding rock compared to the volume of the borehole). However, it is possible that these simplifying assumptions could introduce some uncertainties into the estimated

permeability value. The primary objective of this paper is to analyze these uncertainties, and to refine the estimated permeability values from Paper I. In addition, as a result of this study, we are also able to estimate additional transport parameters from FFTL data.

In FTTL performed in unsaturated fractured rock, the recorded pressure and temperature data communicate the underlying multiphase flow and transport processes in response to the applied perturbation (i.e., pumping of air). A full and complete analysis of FFTL data requires a systematic investigation using a conceptual model that will encompass anticipated multiphase flow and heat-transport processes in a fractured porous medium. These include water and vapor flow, heat transport by conduction and convection, and plausible changes in the physical condition of the rock matrix and fractures surrounding the borehole being pumped. Many of these factors were assumed to be negligible in the conceptual model presented in Paper I, based on intuition and plausibility arguments. In this paper, we reexamine these hypotheses put forth in Paper I, and seek to affirm or negate some of those assumptions, based on a systematic numerical study. This approach is also useful in providing quantitative estimates of uncertainties associated with ignoring a particular process or feature.

In this paper, data from FFTL are analyzed using the numerical flow and transport simulator TOUGH2 [*Pruess*, 1991; *Pruess et al*., 1999]. TOUGH2 is a general-purpose simulation program for multidimensional fluid and heat flows of multiphase, multicomponent fluid mixtures in porous and fractured media. In addition, we conduct statistical analysis of the data and parameter estimation by using the optimization and inversion software package *i*TOUGH2 [*Finsterle*, 1999a,b,c, http://esd.lbl.gov/*i*TOUGH2], which is based on the TOUGH2 code. *i*TOUGH2 has been extensively used in unsaturated and multiphase inverse modeling of both laboratory and field test data; see *Finsterle* [2004] for a review of *i*TOUGH2 applications. More specifically and with more relevance for this paper, *i*TOUGH2 has been successfully used for parameter estimation in gas flow and transport experiments [*Finsterle and Persoff*, 1997; *Ahlers et al*., 1999; *Unger et al*., 2004] and nonisothermal two-phase flow

[*Finsterle et al*., 1998; *Finsterle et al*., 2000; *Engelhardt et al*., 2003; *White et al*., 2003; *Björnsson et al*., 2003; *Finsterle*, 2005; *Zarrouk et al*., 2007].

A model is a simplified, abstracted, and parameterized conceptualization of a natural system. Model conceptualization and parameterization are related [*Finsterle*, 2004], and both are needed to capture and reduce the complexity of the natural system. As long as a process is suitably parameterized, it can be subjected to uncertainty analysis and parameter estimation. Parameterization need not be restricted to hydrologic properties only (in the context of FFTL). It may include aspects of the conceptual model that are considered uncertain (such as the initial and boundary conditions of the model). Even though there is no upper limit to the number of parameters employed for uncertainty analysis, it is not appropriate to determine a large number of strongly correlated parameters for inverse modeling and parameter estimation, given limited data of insufficient sensitivity.

The first step of our investigation is to develop a conceptual model that is a reasonable representation of the multiphase flow and transport processes occurring in the natural system in response to FFTL. Data obtained from an actual FFTL, and other prior information about the natural system (such as permeability of the rock determined from previous independent testing) is used to constrain the model. In the next step, we perform a systematic sensitivity study to determine the parameters that have the strongest influence on a FFTL response. In the last step, we use *i*TOUGH2 for estimation of these parameters and analysis of uncertainties in the estimated values.

2. Recapitulation of FFTL

In FFTL [*Tsang et al*., 2007; *Mukhopadhyay and Tsang*, 2008], air (which intrinsically contains water vapor) is pumped at a constant rate from a packed-off zone in a borehole located in unsaturated fractured rock. In response to the applied perturbation (i.e., pumping of air), air enters the borehole from conducting fractures intercepted by it, and undergoes a change in pressure. As a result, a temperature signal can be measured. If one plots temperature versus borehole depth (a vertical profile plot), a sharp peak will be

observable at the location of the highly conducting fracture. This peak can thus be useful in detecting the locations of discrete fractures within certain resolution. Additionally, a transient plot of borehole temperature can be useful in obtaining estimates of transport properties of the fractured formation [*Mukhopadhyay and Tsang*, 2008].

2.1 Data Collection Process

The FFTL data presented in this paper were collected using a temperature logging tool. Figure 1 shows photographs of the logging tool, the design of which can be found in *Tsang et al.* [2007]. Using inflatable packers, the logging tool can be used to pack off a 0.9 m zone of a borehole at any one time. The logging tool has five temperature sensors (linear thermisters) at a gap of 0.15 m with one another. Out of the five temperature sensors in the logging tool, Sensor #1 is always located at the deepest end of the tool and Sensor #5 is located closest to the end where pumping is applied.

A typical set of FFTL data is shown in Figure 2; the same data were used for the theoretical analysis in Paper I. These FFTL data were collected from a single borehole (Borehole 182) in Alcove 5 of the Exploratory Studies Facility (ESF) at Yucca Mountain, Nevada. The ESF at Yucca Mountain was constructed to facilitate characterization of Yucca Mountain as the site for high-level radioactive waste repository. Alcove 5 is located in the middle nonlithophysal unit (Tptpmn) of the Topopah Spring Tuff at Yucca Mountain. For the sake of completeness, Borehole 182 has a radius (R_B) of 0.038 m. Further details on FFTL data collection can be found in Paper I.

2.2 Sample FFTL Pressure and Temperature Data

Figure 2a shows a sample of the measured pressure response in the borehole during FFTL. Figure 2a also shows the transient pumping rate data that was applied at the borehole for this particular FFTL. Observe that borehole pressure declined sharply after pumping begun, remained more or less constant barring a slightly increasing trend, and then increased sharply back to the original pressure as pumping stopped. Paper I provides a detailed interpretation of borehole pressure response during FFTL – a brief recapitulation of the same is also provided in Section 2.3 (see below).

Temperatures recorded by the five different sensors are shown in Figure 2b. In Figure 2b, Sensor 5 is closest to that end of the logging tool where pumping is applied, and Sensor 1 is the farthest (i.e., zone 1 is situated deepest into the borehole). Except for Sensor 5, temperatures recorded by the other four sensors are similar. All of them exhibit a sharp decline in temperature at the start of pumping before gradually recovering to their original, pre-pumping values. When pumping is stopped, temperatures went above their original values. In other words, cooling was observed in the borehole at the commencement of pumping, and heating trends were observed as pumping was stopped. Contrary to the temperature history recorded by sensors 1 through 4, persistent cooling trends were recorded by Sensor 5 throughout the pumping period, and temperature began to increase only after pumping was stopped. We are yet to find an explanation for this anomalous temperature recording by Sensor 5. One possible explanation could be that, for this particular location, the rock closest to Sensor 5 was relatively less fractured (that could be why temperature dropped in response to pumping but did not rebound because no fracture or fractures were feeding into the borehole at that location). However, to test the above hypothesis, more analysis is needed. Consequently, in the rest of this paper, we will focus on temperatures recorded by Sensors #1 through #4. Note that not including data from Sensor #5 does not impact the rest of the analysis presented in this paper. Note also that, at the beginning of the sample data, Sensor #4 records the maximum temperature, while Sensor #1 records the smallest temperature. The difference between the largest and smallest measured temperatures, however, is small (less than 0.06^{o}C). This small difference can be attributed either to differences between individual sensor's precision or to local heterogeneities.

2.3 Qualitative Interpretation of FFTL Data

A comprehensive interpretation of FFTL data has been provided in Paper I. For the sake of completeness, we provide a brief summary of the same in this paper. When air is pumped from a borehole with fixed volume, both pressure and temperature inside the borehole decrease. This is a situation similar to an adiabatic expansion experiment. If pumping is performed slowly (resembling a reversible process in a thermodynamic

sense), the drop in temperature of a gas will be related to the drop in its pressure. Because the borehole is located in a highly fractured rock, which acts as a source of fluid (air and water in this case), temperature (and pressure) signature from FFTL differs from that of a reversible adiabatic expansion experiment. For example, as pressure drops inside the borehole because of pumping, air (along with water vapor) begins to flow from the fractured rock into the borehole. However, since the fractured rock has a finite permeability, it takes some time (i.e., there is a "lag") before fluid from the rock can reach the borehole, until which time pressure continues to decline. Eventually, pressure inside the borehole equilibrates with the fractured rock (i.e., rate of fluid flow from the rock formation is approximately equal to the rate of pumping), and pressure does not decline any further even if pumping continues.

During the lag period (when pressure is declining in response to pumping), the decrease in borehole temperature can be attributed to adiabatic expansion effects. During this period, enthalpy of the air inside the borehole becomes smaller than that in the fractured formation. It is easy to see that borehole temperature (and enthalpy) will be at its minimum when borehole pressure just about reaches equilibrium with the pressure in the fracture formation (i.e., rate of flow of fluid into the borehole is just about equal to pumping rate). Once pressure has equilibrated, any mass of air that leaves the borehole because of pumping is replaced by an equivalent mass of air from the fracture formation. However, recall that the enthalpy of air leaving the borehole during this time is smaller than the enthalpy of air flowing into it. Consequently, once pressure reaches equilibrium, borehole temperature begins to increase. This process (of rising temperature) continues until equilibrium in enthalpy between the borehole and the fracture formation is established, after which time temperature does not climb any further even if pumping is continued (i.e., both pressure and temperature reaches steady state conditions). In other words, a turnaround (from falling to rising) in borehole temperature is observed during pumping in FFTL in a fracture formation.

The temperature signature (the increase in temperature) after pumping stops can be explained similarly. At the end of pumping, air continues to flow in from the rock

formation (because of residual pressure gradient) causing adiabatic compression (instead of previously observed adiabatic expansion) of air residing inside the borehole, which results in an instantaneous increase in borehole temperature. This process continues until (enthalpy) equilibrium is again established between the borehole and the fracture formation.

2.4 Flow Regime Verification

For the FFTL data presented in this paper, air was pumped at an average rate of approximately 25.2 standard liters per minute (SLPM) or 5.43×10^{-4} kg s^{-1} for 322 seconds. The velocity of air (V) inside the borehole resulting from pumping of air at the rate of $\dot{m}$ (in units of kg s^{-1}) can be approximated from (the actual velocity may be slightly larger because of the reduction of flow area owing to the space occupied by the logging tool)

$$V = \frac{\dot{m}}{\pi R_B^2 \rho} \tag{1}$$

The Reynolds number for flow inside the borehole can then be estimated from

$$\mathrm{Re} = \frac{2R_B V \rho}{\mu} \tag{2}$$

Using Equation 2 in Equation 1 to eliminate **V**, we obtain

$$\mathrm{Re} = \frac{2\dot{m}}{\pi R_B \mu} \tag{3}$$

Thus, with $\dot{m} = 0.543\times10^{-3}$ kg s^{-1}, $R_B = 0.038$ m, and $\mu = 1.86\times10^{-5}$ kg m^{-1} s^{-1}, we obtain a Reynolds number of approximately 490 for flow inside the borehole. The actual borehole Reynolds number may be slightly larger than this because of the reduction of flow space owing to the logging tool volume. However, laminar flow is expected to occur in a cylindrical pipe as long as the Reynolds number is less than 2100-2300. It is unlikely that the borehole Reynolds number will be close to 2100-2300, even if corrections are made for the reduction in flow space. It is therefore reasonable to assume that laminar flow conditions (and a Darcy flow regime) are maintained inside the borehole during the FFTL presented in this paper.

After ascertaining that laminar flow conditions prevail inside the borehole in response to the applied pumping rate, we next verify that laminar flow conditions also persist in the fracture continuum surrounding the borehole. Note that, in this paper as well as in Paper I, the fractured rock outside the borehole has been conceptualized as a porous medium. For flow in a porous medium, it is generally assumed that the characteristic length scale for flow is proportional to the square root of absolute permeability [*Brutsaert*, 2005, pp. 277-278]. Using this assumption, Reynolds number for flow in a porous medium can be estimated from [*Brutsaert*, 2005, see Equation 8.33]

$$\mathrm{Re} = \frac{\sqrt{k}V\rho}{\mu} \tag{4}$$

However, there is one difficulty in using Equation 4, i.e., the flow velocity (V) in the porous medium is not known, and cannot be estimated without assuming an appropriate flow regime (such as the laminar flow regime or applicability of Darcy law). However, because our objective is to ascertain the flow regime itself, making an assumption on the flow regime to estimate V will create a situation of using circular logic.

To circumvent this problem of using circular logic, we assume that the magnitude of flow velocity in the porous medium is equal to the velocity inside the borehole. Note that the actual flow velocity in the surrounding porous medium is likely to be smaller than that inside the borehole (where the pumping is applied directly). Consequently, the estimated porous medium Reynolds number is likely to be larger than the actual porous medium Reynolds number. However, if it is determined that laminar flow regime is prevalent in the porous medium even for this estimated Reynolds number (which is larger than the actual Reynolds number), we can be assured that laminar flow regime persisted under the actual FFTL circumstances.

Using Equation 1, we can estimate the velocity of air V inside the borehole as approximately 0.1 m s^{-1} (using ρ = 1.2 kg m^{-3} as density of air, the values of the other parameters in Equation 1 can be found just after Equation 3). Note that in Paper I we

have estimated the permeability (k) of the fracture continuum as 4×10^{-13} m^2. Using these parameter values in Equation 4, we estimate the Reynolds number in the porous medium as approximately 0.004. As we stated earlier, the actual Reynolds number is likely to be smaller than 0.004 (because we have used a larger flow velocity in the estimation of Reynolds number). For flow in a porous medium, creeping or laminar flow is assumed if the Reynolds number is of the order of 1 [*Brutsaert*, 2005, see pp. 277-279]. Because the estimated Reynolds number is much smaller than 1, we can safely assume that during the FFTL laminar flow regime prevailed in the fracture continuum as well. Because laminar flow prevailed both inside the borehole and in the fracture continuum during FFTL, we will assume that Darcy law is valid for the remainder of the analysis in this paper.

3. Inverse Modeling Approach

The numerical inversion simulator *i*TOUGH2 is used to estimate flow and transport parameters by matching the simulated system response (of pressure and temperature) to measured pressure and temperature data from FFTL. *i*TOUGH2 estimates elements of a parameter vector $\mathbf{p}$ (of length n, the number of parameters to be estimated), based on observations summarized in vector $\mathbf{z}^*$ (of length m), by minimizing an objective function S, which is a function of the residual vector, $\mathbf{r}$. For example, for the inversions presented in this paper, the elements of the vector $\mathbf{p}$ could be hydrological and thermal parameters of the rock (such as permeability, porosity, thermal conductivity, or specific heat capacity) and/or the initial and boundary conditions of the system. Vector $\mathbf{z}$ contains the pressure and temperature data at discrete points in space and time, where the measured quantities are indicated by an asterisk, $\mathbf{z}^*$, and simulated results are represented by $\mathbf{z}$. The residual vector $\mathbf{r}$ contains the difference between the measured and simulated system response; the latter is a function of the parameter vector $\mathbf{p}$. The objective function S is a measure of the misfit between the data and the simulated response. If the residuals ($\mathbf{z}^*$-$\mathbf{z}$) are normally distributed with mean $E[(\mathbf{z}^*-\mathbf{z})]=0$ and covariance matrix $E[(\mathbf{z}^*-\mathbf{z})(\mathbf{z}^*-\mathbf{z})^T] = \mathbf{C}_{zz}$, maximum likelihood theory yields the weighted least-squares objective function:

$$S = \left(\mathbf{z}^* - \mathbf{z}\right)^T \mathbf{C}_{zz}^{-1}\left(\mathbf{z}^* - \mathbf{z}\right) = \mathbf{r}^T \mathbf{C}_{zz}^{-1}\mathbf{r} = \sum_{i=1}^{m} \frac{r_i^2}{\sigma_i^2} \tag{5}$$

The best estimate parameter set minimizes the objective function in Equation 5. While *i*TOUGH2 offers a number of minimization algorithms, the Levenberg-Marquardt [*Levenberg*, 1944; *Marquardt*, 1963] modification of the Gauss-Newton algorithm is used for the inversions in this paper.

The estimated error variance s_0^2 represents the variance of the weighted residuals and is thus a measure of goodness of fit

$$s_0^2 = \frac{\mathbf{r}^T \mathbf{V}_{zz}^{-1}\mathbf{r}}{m-n} \tag{6}$$

where $\mathbf{V}_{zz}^{-1}$ is a weighting matrix such that

$$\mathbf{C}_{zz} = \sigma_0^2 \cdot \mathbf{V}_{zz} \tag{7}$$

While σ_0^2 can assume any positive value, it is convenient to set $\sigma_0^2 = 1$, i.e., the weighting matrix is the inverse of the covariance matrix.

4. Model Development

A fractured rock formation normally consists of a rock matrix continuum (having low porosity and low permeability, a fracture continuum (consisting of many small and large interconnected fractures, with permeability which is considerably larger than that of the rock matrix continuum), and few large discrete fractures with very large permeabilities (permeabilities that are larger than even that of the fracture continuum). To begin with, we assume that the rock is not at all fractured (i.e. it has no fracture continuum or any discrete fracture), and that it is absolutely impervious (i.e., it has zero permeability). If air is pumped from a borehole located in such a rock, temperature (and pressure) in the borehole will decline continuously (because no air is supplied to the borehole from the rock which has zero permeability) until all the air is pumped out.

Let us now introduce a single high-permeable discrete fracture, which is narrow and thin, into the otherwise impervious rock. Because the discrete fracture has a very high permeability, it will bring in some amount of air into the borehole. However, this single discrete fracture, because it is thin and narrow, can bring in only a very small amount of air. Thus, the pressure and temperature in the borehole will decline in almost the same manner as in the previous case (no discrete fracture and impervious rock). If we plot temperature versus location in the borehole at different times, we will see rapidly declining temperatures at all locations except at the location of the discrete fracture, which will be held at more or less the constant initial temperature (because of its very fast communication with the boundary, resulting from its high permeability). As a result, the temperature data from FFTL can indicate the locations of high-permeability discrete fractures (see Paper I for further discussion).

The presence of the fracture continuum makes interpretation of FFTL data more challenging. Because the fracture continuum has a larger permeability than the matrix continuum, it can supply air into the borehole relatively quickly. At the same time, since the fractures in the fracture continuum are more numerous in number than the occasional large discrete fractures, they can supply substantially more mass of air into the borehole, compared to the few discrete fractures. As a result, FFTL performed in fractured rock produces the types of temperature signatures (initially declining and then increasing) that we discussed earlier (and presented in Figure 2). To analyze these FFTL data, we therefore start with a conceptual model that consists of both a fracture continuum and matrix continuum.

4.1 Fracture Continuum

As discussed in Section 2, FFTL data were collected from the Tptpmn stratigraphic layer at Yucca Mountain. The fracture network at the Tptpmn consists of a well-developed orthogonal set of planar fractures [*Buesch and Spengler*, 1998]. Extensive air-injection testing, aimed specifically at providing estimates for fracture properties, has been performed in the Tptpmn unit [*Freifeld*, 2001]. For example, air-injection testing was

carried out in 31 different boreholes near the location of the Single Heater Test [*Huang et al*., 1999; *Tsang and Birkholzer*, 1999] at the ESF. From these air-injection tests, *Huang et al*. [1999] reported that the Tptpmn rock is highly heterogeneous with fracture permeability varying between 1×10^{-15} to 8×10^{-11} m^2 (with a geometric mean of 1×10^{-13} m^2). Air-injection tests [*Birkholzer and Tsang*, 2000; *Freifeld*, 2001] were also carried out at 46 different zones in 12 boreholes near the location of the Drift Scale Test (DST) [*Birkholzer and Tsang*, 2000; *Mukhopadhyay and Tsang*, 2003]. From these tests, it was reported [*Birkholzer and Tsang*, 2000; *Freifeld*, 2001] that the fracture permeability varies almost three orders of magnitude, between 1.6×10^{-15} and 9.7×10^{-13} (with a geometric mean permeability of 1.3×10^{-13} m^2). As far as gas flow is concerned, at the scale of ~10 m, the fractures at the Tptpmn are well connected, forming a continuum [*Birkholzer and Tsang*, 2000]. This is further supported by tracer test data [*Freifeld*, 2001], because the gas tracer breakthrough curves are smooth, displaying none of the multiple peak signatures that characterize discrete flow channels [*Moreno and Tsang*, 1991]. Assessing the appropriateness of a continuum model description for the Tptpmn on the scale of a few meters is not a trivial problem [*Freifeld*, 2001]. However, in the absence of evidence suggesting otherwise, we will rely on the observed evidence and adopt a continuum description for Tptpmn fractures.

4.2 Matrix Continuum

The porosity of the Tptpmn matrix is typically 0.11 with a standard deviation of 0.01 [*Ghezzehei and Liu*, 2004]. The Tptpmn rock matrix is quite wet, with a typical water saturation value of 92% [*Tsang and Birkholzer*, 1999]. The mean absolute permeability of the Tptpmn matrix is estimated to be 4.5×10^{-19} m^2 with a standard deviation of 0.97 in log10 space [*Ghezzehei and Liu*, 2004]. Because of the typically high water saturation (~92%), the effective gas-phase permeability of the Tptmn matrix is likely to be considerably less than the absolute permeability of 4.5×10^{-19}. On the other hand, since the fractures are almost dry (typical liquid saturation being 2-5%, see *Ghezzehei and Liu* [2004] and references therein), the effective gas-phase permeability in the fractures is on the order of 10^{-13} m^2 (because gas-phase relative permeability in the fractures is close to unity). In other words, the gas-phase effective permeability of the matrix is

approximately six orders of magnitude lower than that of the fractures. Given these large contrasts in effective gas-phase permeability values for the fracture and the matrix, and also the short duration of testing typically associated with FFTL, it is unlikely that, except in the immediate vicinity of the borehole [*Illman and Neuman*, 2001; *Illman and Neuman*, 2003], gas transport from the matrix will have a significant impact on the pressure and temperature response recorded in the borehole. Thus, while analyzing the pressure and temperature data from FFTL, it is justified to exclude the matrix continuum from the conceptual model. In a future paper, we intend to analyze the flow behavior in the matrix continuum in the immediate vicinity of the borehole.

4.3 Numerical Grid and Boundary Conditions

A schematic representation of the conceptual model for FFTL can be found in Figure 3. The borehole has a radius of R_B and a permeability of k_B, and a packed-off zone of length H as shown in Figure 3. The borehole is surrounded by fractured rock with an effective continuum permeability of k_C. For the sake of simplicity and the semi-analytical solution that follows, we will assume that the borehole is intersected by one discrete fracture having a permeability of k_F, with the implicit assumption that $k_B >> k_F >> k_C$. The origin of the coordinate system is located at the bottom of the packed-off zone ($z=0$). The discrete fracture is located at $z=h$, and pumping is applied at $z=H$, i.e., $H > h$. Constant pumping at the rate of $\dot{m}$ is applied at the top (i.e., $z=H$) of the packed-off zone. Before pumping starts (i.e., at t=0), the fracture continuum, the discrete fracture, and the borehole are at constant temperature T_i and constant pressure P_i.

To conduct the forward and inverse simulations of FFTL, we created a radial-axial numerical grid. The grid consists of the entire length of the packed-off zone (0.9 m) in the axial (z) direction. There were 36 equal divisions in the z direction such that each division is 0.025 m in length. Inside the borehole, the grid was not discretized radially. In other words, the borehole was represented by 36 cylindrical grid segments, each of 0.038 m radius (equal to the radius of the borehole) and 0.025 m length. Extensive sensitivity studies were performed (though results are not shown here) which indicated that this level of grid refinement was adequate and computationally optimum.

Outside the borehole (i.e., in the fracture continuum), the axial gridding was maintained at 0.025 m. The radial gridding started with increments of 0.038 m. As the radial distance increased from the borehole, the radial increments increased logarithmically. The radial extent of the numerical grid (i.e., the location of the outer radial boundary) is part of the first set of sensitivity studies and will be discussed in the next subsection. No-flow boundary conditions were applied at the two axial ends ($z = 0$ and $z = H$) of the numerical grid. Constant pressure and temperature boundary conditions were applied at the outer radial boundary. Pumping was applied in the borehole element at $z = H$.

4.4 Location of Constant Pressure Boundary

When pumping is applied during FFTL, air (plus water vapor) moves out of the borehole, and is replenished by air (plus water vapor) coming in from the fractured rock. Because the permeability of the borehole is several orders of magnitude larger than that of the fracture continuum, the distance of the outer boundary (constituting the source) from the borehole being pumped has a significant impact on the pressure and temperature response from FFTL. The farther this constant pressure boundary is from the borehole, the larger the time lag for the pressure sensor within the borehole to realize its communication with the source. As a result, pressure (and subsequently, temperature) at the borehole under such circumstances will drawdown over a longer time compared to the case in which the constant pressure boundary is closer to the borehole (assuming identical permeability for both cases). In the following, we analyze the pressure signal from FFTL to determine the appropriate location of the placement of the constant pressure and temperature boundary in our simulations.

Forward simulations were performed with the TOUGH2 simulator [*Pruess* 1991; *Pruess et al*., 1999] by placing the constant pressure (and temperature) boundary initially at a radial distance of 100 m, and gradually bringing it to 10, 1, 0.1, or 0.01 m. The numerical grid for these four simulations is otherwise the same. Hydrological and thermal properties of the fracture continuum used in these simulations are tabulated in Table 1. These parameter values are typical of the Tptpmn unit and previously estimated through various methodologies [*Huang et al*., 1999; *Tsang and Birkholzer*, 1999; *Birkholzer and Tsang*,

2000; *Ghezzehei and Liu*, 2004]. The permeability of the fracture continuum is assigned to be 4.0×10^{-13} m^2, estimated using the semi-analytical solution in Paper I. Also, the measured transient pumping-rate was applied in all these simulations. In Figure 4, simulated pressure response in the borehole is compared with the measured pressure signal. When the constant boundary is situated at 100 or 10 m, the simulated pressure continues to decline over the duration of pumping (322 seconds). On the other hand, when the boundary is placed at distances of 0.1 or 0.01 m, the simulated pressure exhibits much smaller drawdown than what has been measured. Measurements, however, show that the pressure, after declining for less than 10 seconds, reaches steady state quickly (no further drawdown in borehole pressure). Such a pressure drawdown behavior can only be reproduced if the constant boundary were close to 1 m. *Illman* [2005] reached a similar conclusion while analyzing single-hole tests in fractured tuff. For simulations presented in the rest of the paper, we thus place the constant pressure and (temperature) boundary at a radial distance of 1 m.

Another feature of the transient pressure behavior (see Figure 4) requires further elaboration. The measured pressure shows a sharp decline at the start of pumping. During the pumping period, measured pressure exhibits a slight upward trend. After pumping ends, pressure rapidly builds up to pre-pumping levels. While the overall transient pressure behavior is captured in the simulations, the slight increasing trend during pumping is not captured. The slightly increasing trends of measured transient pressure behavior could have resulted from a variety of reasons.

1. It could have resulted from condensation of water vapor from saturated air as it entered the borehole from the fractured formation in response to pumping. This effect has been included in the conceptual model, but the increase in simulated pressure resulting from this is less than what is observed in measured pressure data.

2. It is possible that the decreasing trends of pumping rate resulted in a gradual increase in pressure after the initial sharp drawdown. This effect (decreasing pumping rate) has also been included in the conceptual model. However, the simulated pressure rise is not as evident as the measured one.

3. The pressure increase during pumping might have resulted from leakage issues. *Guzman et al*. [1996] and *Illman and Neuman* [2000,2001] have observed similar effects while performing single- or cross-hole air injection testing in fractured tuff at the Apache Leap Research Site. However, assuming this is indeed true, we do not have enough information regarding leakage to investigate this issue more quantitatively.

4. A more likely possibility is that the presence of instrumentation and data collection system (such as the sensors) inside the borehole resulted in a reduction of actual air volume inside the borehole, which may have contributed to the slight increase in measured pressure. However, there is uncertainty in how much reduction in volume actually happened because of the instrumentation, and thus this could not be investigated quantitatively. We may investigate this matter more in future.

In summary, it is true that there is some unresolved uncertainty regarding the slightly increasing trend in pressure during pumping. This uncertainty could not be quantified without investigating further processes (such as leakage) or without obtaining more information (such as the extent of volume reduction because of borehole instrumentation). Overall, however, the pressure rise is small during the pumping period (in comparison to the large initial drop in response to pumping or the sharp increase in pressure when pumping ended). Thus, while not including this increasing trend in pressure in the conceptual model may have introduced some uncertainty, such uncertainty is expected to be small.

4.5 Equation of State

In the TOUGH2 simulator [*Pruess*, 1991; *Pruess et al*., 1999], there are two primary modules (EOS3 and EOS4) to describe equations of state for air-water systems. In both modules, water properties are represented by the steam table equations as given by the *International Formulation Committee* [1967]. Air is approximated as an ideal gas, and additivity is assumed for air and water vapor partial pressures in the gas phase. The viscosity of air-vapor mixtures is computed from a formulation given by *Hirschfelder et al*. [1954]. The solubility of air in liquid water is represented by Henry's law, with a

Henry's law constant of 1×10^{10} Pa, assumed independent of temperature [*Loomis*, 1928]. The EOS4 module differs from the EOS3 module in that provision is made for vapor pressure lowering effects. In the EOS4 module, vapor pressure is calculated from Kelvin's equation (see Equations A.7 and A.8), which is a function not only of temperature but also of capillary pressure. Since it is known that porous medium flow involving air and water phases involves vapor pressure lowering effects, unless otherwise stated, all forward and inverse simulations in this paper have been performed with the EOS4 module in preference to the EOS3 module.

5. Parameter Selection through Forward Modeling

A large set of hydrological and thermal parameters may influence FFTL response in unsaturated fractured rock. Some of these parameters are intrinsic permeability, porosity, gas- and liquid-phase relative permeability and capillary pressure characteristics (including all the parameters of any selected relative permeability and capillary pressure versus saturation function), initial and boundary pressure, water (or gas) saturation, and temperature, thermal conductivity, and specific heat capacity. While it is possible in principle to estimate through inverse modeling most, if not all, of these parameters from the pressure and temperature data recorded by FFTL, doing so may not be desirable (as discussed in Section 1). We therefore first perform forward simulations to determine which parameters have the strongest influence on FFTL. We then subject those parameters to inverse modeling and parameter estimation. Inverse modeling will be discussed in Section 6. In this section, we focus on parameter selection through forward simulations.

All the forward simulations in this paper were performed using *i*TOUGH2 [*Finsterle*, 1999a,b,c] in forward mode, which is essentially equivalent to using the TOUGH2 simulator [*Pruess*, 1991; *Pruess et al.*, 1999]. For the sake of completeness, the differential equations solved by TOUGH2 or *i*TOUGH2 for multiphase, multicomponent transport of fluids and heat are provided in Appendix A. Heat transport is both by conduction and convection, and includes the effects of latent heat arising out of phase change, if any, of water. The differential balance equations in TOUGH2 are solved using

an integral finite-difference approach [*Narasimhan and Witherspoon*, 1976; *Pruess and Narasimhan*, 1985] for spatial discretization. TOUGH2 uses a fully implicit scheme for temporal discretization.

5.1 Specific Heat Capacity

To assess the sensitivity of the temperature response from FFTL to the specific heat capacity of the fracture continuum, we performed simulations with five different values of the specific heat capacity: 600, 800, 1000, 1200, and 1400 J kg^{-1} K^{-1}. The rest of the hydrological and thermal properties are maintained as shown in Table 1. There is virtually no impact (simulation results not shown) on the temperature response as specific capacity is changed by a factor of more than two (from 600 to 1400 J kg^{-1} K^{-1}). This is expected, since the heat storage capacity per unit volume of the fracture continuum [$(1-\phi)\rho_R C_R T$] is considerably larger than that of air [$\phi\rho_a C_V T$], even at the lowest assumed value of 600 J kg^{-1} K^{-1}. The specific heat capacity of the Tptpmn rock is well constrained, and is not expected to assume values outside of the range tested here. It is therefore reasonable to conclude that FFTL temperature response is not sensitive to the specific heat capacity of the formation. Conversely, to determine specific heat capacity from FFTL, more precision in measurement is needed.

5.2 Liquid Saturation

The fracture continuum in the Tptpmn stratigraphic unit is essentially dry. Liquid saturation in the fractures has been estimated to be only 2–5% [*Ghezzehei and Liu*, 2004]. Note that the fracture saturation estimates resulted from inversion of the measured matrix saturation and water potential data using a dual-continuum [*Pruess*, 1991] model, which included matrix permeability, fracture and matrix van Genuchten α, and the active fracture parameter (γ) as calibration parameters. A number of forward simulations were performed with the fracture continuum properties listed in Table 1 but with varying initial liquid saturation between 2% and 15%. The simulated pressure and temperature responses (results not shown) are not sensitive to liquid saturation, at least up to 15% saturation. Since the Tptpmn fractures are not close to 15% saturation, we can leave out

initial liquid saturation from the parameter set that will be subjected to inverse modeling. In the rest of the analysis, the fracture continuum will be assumed to be initially 5% saturated with water, which is a typical value for Tptpmn fractures [*Ghezzehei and Liu*, 2004].

5.3 Parameters Controlling Gas-Phase Relative Permeability

Since the gas-phase Darcy velocity is controlled by the relative permeability in the gas phase, gas-phase relative permeability can be important for permeability estimates from FFTL data. Gas-phase relative permeability is a function of the gas (or liquid) phase saturation, and different functional forms have been developed to describe the dependence of gas-phase relative permeability on (gas or liquid) saturation. For fractured porous media, some of the most widely used functional forms can be found in *Corey* [1954], *Brooks and Corey* [1964], and *van Genuchten* [1980]. We need to select a gas-phase relative permeability function, and also need to determine the sensitivity of the parameters of the selected function towards FFTL data.

For the fractured porous medium of the Tptpmn unit, the irreducible liquid saturation (S_{lr}) has been often reported as 0.01 [*Ghezzehei and Liu*, 2004]. Calibration of water saturation data in the fracture network of Tptpmn has yielded a mean van Genuchten [*van Genuchten*, 1980] exponent (λ) of 0.633. For these typical values, we get a gas-phase relative permeability larger than 0.9 in the liquid saturation range of 2–5% [*Lenhard et al.*, 1989]. Since the fracture saturation does not change by any significant amount during FFTL, except may be in the immediate vicinity of the pumping interval [*Illman and Neuman*, 2001; *Illman and Neuman*, 2003], it is reasonable to conclude that gas-phase relative permeability in the fracture continuum will likely be always larger than 0.9. We thus select the van Genuchten [*van Genuchten*, 1980] model (see Equation A.11) for gas-phase relative permeability, as the uncertainty introduced by selecting one model over the other is expected to be relatively small (less than ten percent). In addition, since gas-phase relative permeability remains close to unity, it is justified not to include the parameters of the relative permeability model in the parameter estimation process. The underlying assumption is that the estimated permeability from FFTL should be

interpreted as the effective gas permeability of the fracture continuum. Note also that hysteresis effects have not been included in the relative permeability estimates.

5.4 Capillary Pressure Characteristics

In FFTL, flow and transport happens mainly in the gas phase, and flow in the liquid phase is relatively less dominant. Consequently, capillary pressure, which plays a dominant role in liquid-phase flow, is not expected to have a significant impact on FFTL. Since we have already selected the van Genuchten model for gas-phase relative permeability, we select the same model for capillary pressure as well (see Equation A.10). The capillary pressure parameters are set such that the relative humidity in the gas phase of the fracture continuum is maintained at close to 100%. When capillary pressure increases, water molecules prefer to stay in the liquid phase, reducing relative humidity in the gas phase. It can be easily verified that, for a van Genuchten type of capillary characteristics function and fracture capillary strength parameter ($1/\alpha$) values in the range of 500 to 10000 Pa, the relative humidity of the gas-phase remains close to 100% at 24°C (the temperature at which the FFTL in this paper was performed) for $\lambda = 0.633$, $S_{lr} = 0.01$, and saturations larger than 2%. In order for the relative humidity to drop to 95% (at a liquid saturation of 5%), or 90% (at a liquid saturation of 2%), ($1/\alpha$) value has to be as large as 1.0×10^{6} Pa (i.e., two to three orders of magnitude larger than any typical value reported so far). Since the fracture ($1/\alpha$) parameter of the Tptpmn unit has been reported to be in the 500-10000 Pa range [*Finsterle et al., 2003*], it is reasonable to conclude that relative humidity in the fracture continuum will remain close to unity for any typical value of ($1/\alpha$). The analysis presented in the rest of this paper is thus performed with a fracture ($1/\alpha$) value of 1000 Pa.

5.5 Other Uncertainties

There are other parameters in our numerical model that, if excluded from the parameter estimation process, may introduce undetected bias in the estimated parameters. First, the active fracture model [*Liu et al.*, 1998] has been routinely used for analyzing and modeling unsaturated flow in Yucca Mountain fractured rock. Since the active fracture model is relevant for liquid water flow in fracture networks, and since flow primarily

occurs in the gas phase in FFTL, we have excluded the parameters of the active fracture model from the parameter estimation process. Second, FFTL data may have been biased by any skin effect or formation damage near the borehole. Such effects have not been parameterized in our conceptual model. Third, the impact of atmospheric pressure and temperature variation on collected data has not been included in the conceptual model. Fourth, some uncertainties remain regarding the appropriate radius of influence around the borehole and calculation of gradient within the radius of influence. Fifth, heterogeneities (in fracture properties) at smaller scales (< 1 m) have not been included in the conceptual model. Finally, the (relatively small) volume occupied by borehole instrumentation and its heat capacity has not been accounted for in the model. These may also have introduced some bias in the estimated transport properties.

6. Sensitivity Analysis and Parameter Estimation

6.1 Sensitivity Analysis

In Section 5, we argued that specific heat capacity, initial liquid saturation, and parameters for saturation dependence of gas-phase relative permeability and capillary pressure can be excluded from the set of parameters to be estimated from FFTL. The parameters that have not been excluded, and that are likely to influence FFTL response, are permeability, porosity, thermal conductivity, initial pressure, and initial temperature. Since the fractures are only 2–5% saturated with water and are essentially dry, we assume that the estimated thermal conductivity in the analysis presented below represents the dry thermal conductivity of the fracture continuum.

Before performing the inversions of pressure and temperature data from an actual FFTL, we used *i*TOUGH2 [*Finsterle*, 1999a,b,c] to perform a more formal sensitivity analysis. Such analysis allows us to determine the contribution of individual data sets to the estimated parameters. A scaled sensitivity matrix $\mathbf{S}$ can be defined, where element S_{ij} is the partial derivative of the calculated system response z_i with respect to parameter p_j, scaled by the inverse of the respective standard deviations, i.e.,

$$S_{ij} = \left(\frac{\partial z_i}{\partial p_j} \right) \left(\frac{\sigma_{z_i}}{\sigma_{p_j}} \right) \tag{8}$$

The scaled dimensionless sensitivity coefficients are shown in Figures 5a and 5b. Figure 5a shows the sensitivity of pressure for each of the five parameters (permeability, porosity, thermal conductivity, initial pressure, and initial temperature) at various times. The sensitivity of calculated state variables (i.e., pressure and temperature) to selected parameters changes with time. For pressure response, permeability is the most sensitive parameter. Of the remaining parameters, the initial pressure moderately influences the calculated pressure response. Knowing the initial pressure accurately will therefore increase the accuracy of the estimated hydrological parameters. Pressure response exhibits a transient sensitivity to porosity at the beginning of pumping, which disappears after steady state has been reached. As expected, thermal conductivity and initial temperature have negligible impact on pressure response.

Figure 5b shows the scaled sensitivity coefficients of the calculated temperature response as a function of time for each of the selected parameters. These scaled sensitivity coefficients are for the temperature response as recorded by Sensor #1 of the FFTL. The sensitivity coefficients for temperature data from Sensors #2, 3, and 4 are similar, and hence are not repeated here (see discussion of Figure 6 below). Temperature response is influenced most strongly by permeability and initial temperature. However, unlike sensitivity of pressure, sensitivity of temperature to permeability appears to increase with time during pumping, which is followed by an abrupt decline as pumping stopped. Temperature exhibits considerable sensitivity to thermal conductivity immediately after commencement of pumping (when there is maximum difference in temperature between the borehole and the fracture continuum, resulting in the largest conductive flux of heat into the borehole). Temperature also exhibits some sensitivity to porosity at the beginning and end of pumping (which is different from sensitivity of pressure to porosity). Temperature shows little sensitivity to initial pressure, which is expected.

Figure 6 presents essentially the same data as in Figure 5, but in a different format. For each of the five selected parameters, Figure 6 shows the total (i.e., sum of absolute values over all times) scaled sensitivity coefficients for each data set, i.e., pressure and temperature. Note that the scaled sensitivity for temperature for these four sensors is the same, because we have assumed the same rock properties for the entire packed-off zone of 0.9 m.

As discussed earlier, among the rock properties (permeability, porosity, and thermal conductivity), both pressure and temperature responses have the strongest sensitivity to permeability, followed by porosity (though the sensitivity to porosity is orders of magnitude smaller than that to permeability). Sensitivity of temperature response to thermal conductivity is similar (in order of magnitude) to that of porosity. In other words, the pressure and temperature responses from FFTL in the unsaturated fractured rock of Tptpmn are most influenced by three hydrological and thermal parameters: permeability, porosity, and thermal conductivity. The initial temperature and initial pressure also have impact on temperature and pressure response, respectively. However, these are not rock properties and are constrained by measurement. Any error in measuring these two quantities will likely influence the estimated hydrological and thermal properties of the rock.

6.2. Parameter Estimation

The primary objective of the inverse modeling exercise presented in this paper is to focus on discussing the information content of the measured data, and how it can be extracted through process understanding and process modeling. While any inverse modeling exercise needs to be concerned about the uniqueness of the solution, exhaustively examining the issues of uniqueness, and sufficient and necessary conditions, however, is beyond the scope of this paper. Insightful discussion on the uniqueness problem in inverse modeling, particularly to those related to groundwater flow, can be found in *McLaughlin and Townley* [1996], *Zimmerman et al.* [1998], and *Beven* [2006]. Uniqueness issues specific to multiphase inverse modeling by the *i*TOUGH2 code have

been extensively investigated in *Finsterle and Persoff* [1997], and *Finsterle and Faybishenko* [1999].

Before proceeding with the interpretation of experimental data and the actual parameter estimation process, an assessment of the pumping-rate data is needed. The measured pumping-rate data (shown in Figure 7) fluctuated somewhat over time and also exhibited a decreasing trend. The exact reason for this decreasing trend is not known. It is possible that the decreasing trend is related to the slightly increasing trend in measured pressure (see Figure 2a), which in turn may be related to the reduction in borehole volume caused by borehole instrumentation (not included in the conceptual model). To ensure that the fluctuations in the measured pumping rate do not systematically bias the parameter estimation process, we smoothed these data using linear regression (also shown in Figure 7). Note that a quadratic regression (results are not shown here) was also attempted but the simulated FFTL response with the linear and quadratic regressions were similar, and thus the quadratic regression was not selected for further analysis of FFTL data. Note also that the first measured pumping-rate value was excluded from the smoothing process (it was, however, included in the simulations). To illustrate the impact of smoothing the pumping rate, we show the borehole pressure and temperature from two simulated FFTLs in Figure 8. One of the simulations was performed with the actual pumping-rate data, while the second one was performed with the smoothed pumping-rate data. For the sake of easy comparison, Figure 8 also shows the measured pressure and temperature response from the actual FFTL. Note that the simulated pressure and temperature response with the smoothed pumping-rate data are similar to those with the actual pumping-rate data, except for the small-scale fluctuations (which are expected). Consequently, we use the smoothed pumping-rate data in the remainder of the analysis in this paper.

Of the five parameters included in the sensitivity analysis in Section 6.1, only the initial pressure and temperature can be measured directly. Initial pressure and temperature in the borehole can be interpreted as the pressure and temperature, respectively, which were at equilibrium with the rock formation at the beginning of the FFTL. The FFTL data that we are analyzing in this paper were collected between 13:19:00 and 13:28:00 hours on August 6, 1998 [*Tsang et al*., 2007], i.e., over a period of nine minutes. The whole FFTL,

in which an entire borehole (of 20 m length) was logged, lasted slightly over six hours, beginning at 08:20 hours on August 6, 1998 [*Tsang et al*., 2007]. Thus the pressure and temperature that we observe at the beginning of a subset of FFTL data (see Figures 2a and 2b) may not be the actual pressure and temperature that were in equilibrium with the formation. To obtain these equilibrium pressure and temperature, one may have to consider the measured data at the beginning of the FFTL.

As an example, we present the temperatures recorded by the four sensors over the entire duration (22062 seconds) of the FFTL in Figure 9. From this figure, one can estimate that the initial temperature was close to 24.1^{o}C. However, when we consider only a subset of the FFTL data, the estimate of initial temperature may be different. This is illustrated in the inset of Figure 9, where we show the FFTL data between 17875 and 18200 seconds (these are the data that we are analyzing in this paper). If one had access to only the data in this inset, one would have estimated the initial temperature as 24.2^{o}C (ignoring the small difference in temperatures recorded by the four sensors). A different subset of the FFTL data, collected at a different time of the day, might have resulted in a different estimate of initial temperature. While the difference between estimated initial temperatures is not large (~0.1^{o}C), such uncertainty can have some impact on estimated parameters from FFTL. This is particularly true because the overall magnitude of temperature drop from a FFTL is expected to be on the order of 0.5^{o}C. Thus, an uncertainty of 0.1^{o}C in estimating the initial temperature of the borehole (and the formation) can be significant. In the following, we will illustrate the influence of this uncertainty on the estimated parameters.

We initially performed an inversion by assuming that the initial temperature and pressure are known. We assumed that the initial pressure is 85500 Pa and initial temperature is 24.2^{o}C. Figure 10 shows the measured pressure and temperature (from all four sensors), along with the best-fit simulation results. The best-fit simulated pressure response agrees quite well with the measured pressure response. On the other hand, the best-fit simulated temperature drop does not match the measured temperature data as well. More specifically, the maximum temperature drop predicted by the simulations at the onset of

pumping is smaller than the temperature drop recorded by any of the four temperature sensors. The converse is true about the rise in temperature at the end of pumping, i.e., simulated temperature rise at that time is larger than any of the measured data. Overall, the simulated temperature response matches the measured temperature data from Sensor #2 best.

The best-fit parameter estimates are shown in Table 2. Note that the best-fit values and the standard deviations for permeability and porosity are given in log10 space. The best-fit estimate for log-permeability is –12.48 (3.3×10^{-13} m^2), which agrees well (consider also the small σ_p value of 0.03 for log-permeability) with the estimation from the semi-analytical solution in Paper I (3.9×10^{-13} m^2). It is also in good agreement with other independent estimates of fracture permeability in the Tptpmn unit [*Huang et al*., 1999; *Birkholzer and Tsang*, 2000; *Freifeld*, 2001]. The best-fit log-porosity estimate is –1.37 (0.043), which is significantly larger than any previous estimates [*Freifeld*, 2001]. On the other hand, the best-fit thermal conductivity is 1.47 W m^{-1} K^{-1}, which is consistent with the dry thermal conductivity values of Tptpmn estimated previously [*Brodsky et al*., 1997; *Mukhopadhyay et al*., 2007].

The statistical correlation coefficients of the estimated parameters were also evaluated. *i*TOUGH2 calculates the ratio of the conditional estimation uncertainty σ_p^* and the marginal estimation uncertainty σ_p, which can be interpreted as an overall measure of how independently a parameter can be estimated [*Finsterle and Persoff*, 1997]. If this ratio is small, the estimated parameters are highly correlated. This ratio is also a measure of how well-posed the inverse problem is. A value of this ratio close to unity indicates the relatively well posed. As shown in Table 2, this ratio is close to unity for our case for the three estimated parameters, which implies that the estimated parameters are weakly correlated and can be estimated independently, and the inverse problem is well posed. Table 2 also shows the sensitivity of the objective function to the estimated parameters. As was discussed in Section 6.1, permeability has the strongest influence on the pressure and temperature response from FFTL.

We conducted a second set of inversions of FFTL data where, in addition to the three parameters above, initial pressure and initial temperature were also included in the parameter estimation process (i.e., it is assumed that these parameters are not known). The best-fit pressure and temperature response from this inversion is shown in Figure 11. We note that the model response to pressure data does not change much with the inclusion of two additional parameters in the estimation process. However, the fit to temperature data changes considerably from the previous inversion (see Figure 10). The best-fit parameter estimates from this inversion are given in Table 3. The best estimate of permeability remains virtually unchanged (at 3.3×10^{-13} m^2) from the previous inversion. However, porosity estimate changes significantly from the last estimate. The new estimate (-2.04 in log10 space or 0.009 or 0.9%) is similar to what has been reported previously [*Freifeld*, 2001; *Ghezzehei and Liu*, 2004] for Tptpmn fractures. The best-fit estimate for (dry) thermal conductivity is 1.67 W m^{-1} K^{-1}, quite similar to the routinely used values of dry thermal conductivity for the Tptpmn stratigraphic unit [*Brodsky et al.*, 1997; *Tsang and Birkholzer*, 1999; *Birkholzer and Tsang*, 2000; *Mukhopadhyay and Tsang*, 2003; *Ramsey et al.*, 2004; *Mukhopadhyay et al.*, 2007]. For the sake of convenience, Table 4 provides a comparison of the estimated parameter values (for permeability, porosity, and thermal conductivity) with previous independent estimates. Table 4 also provides a brief description of the methodologies used in obtaining the parameter estimates. This latter inversion also estimated an initial pressure of 85547 Pa (with a σ_p of 83 Pa), and an initial temperature of 24.15^{o}C (with a σ_p of 0.003^{o}C). From Figure 8, we note that the recorded temperature over the first several minutes was around 24.12^{o}C, which possibly was the fracture continuum temperature at the beginning of the FFTL. It is thus useful to include the initial pressure and initial temperature in the estimation process.

The statistics for this latest inversion provides useful insights. When we compare the results of this inversion with those of the previous inversion, we see that the marginal estimation uncertainty σ_p is similar for permeability. However, σ_p is larger for both porosity and thermal conductivity in this latest inversion because these parameters are

moderately correlated to each other, which is in contrast to the previous inversion where these parameters were weakly correlated. Based on this analysis, we recommend that, because initial pressure and initial temperature influence the estimated fracture properties, these two parameters be gathered at the start of the FFTL, and not obtain it from a subset of FFTL data. Though not included in this paper, we believe that the estimate of parameters from FFTL can be further improved if the conceptual model also accounts for additional processes, such as atmospheric variations in pressure and temperature. We will like to address these issues in a future paper.

In summary, pressure and temperature data from FFTL can be used to determine hydrological and thermal parameters of the host rock. If a quick estimate of the fracture-network permeability is needed, the semi-analytical solution in Paper I can be used. As the analysis in this paper has illustrated, the estimate of permeability from the semi-analytical solution, even though based on certain simplifying assumptions, is quite reliable. On the other hand, a complete analysis of FFTL data provides further insight into flow and heat transport in fractured unsaturated rock, and can be used to estimate – in addition to permeability – porosity, thermal conductivity, and initial pressure and initial temperature of the rock.

7. Conclusions

In a recent paper [*Mukhopadhyay and Tsang*, 2008], based on a simplified conceptualization of single-phase flow of air, we developed a semi-analytical solution to determine spatial and temporal variations of pressure and temperature in response to applied perturbation (i.e., pumping of air) at a borehole located in unsaturated fractured rock. Using this semi-analytical solution, we proposed a method for determining the permeability of the fracture continuum from the temperature data from FFTL. The estimated effective fracture continuum permeability of the DST host rock, using our proposed method, compared well with previous independent estimates.

The model conceptualization of FFTL in Paper I was based on various simplifying assumptions. Thus, while such simplified representation of FFTL provided meaningful

insight into the underlying physics of flow and transport, a more comprehensive conceptualization of FFTL in unsaturated fractured rock was needed. This is what is accomplished in this paper. We developed a numerical model of multiphase flow and heat transfer associated with FFTL, using the TOUGH2 simulator. We performed a series of forward simulations to select the parameters that have significant influence on the pressure and temperature response from FFTL. These selected parameters were then subjected to inverse modeling using the *i*TOUGH2 optimization and inverse modeling code.

We observe that, of the various transport properties of unsaturated fractured rock, permeability has the strongest influence on pressure and temperature response of FFTL. The other two transport parameters that have significant impact on FFTL response are porosity and thermal conductivity. Using the pressure and temperature data from FFTL performed in the unsaturated fractured rock of the DST, we estimated these three parameters though inverse modeling. The estimated parameter values were comparable with other independent estimates of these parameters. The fracture permeability estimated through inverse modeling is also similar to that obtained from the simplified model presented in Paper I. In other words, if a quick estimate of permeability were needed, Equation 18 of Paper I is a reliable approximation, and elaborate inverse modeling may be omitted. However, the numerical model and the inverse modeling approach presented in this paper are needed for estimating parameters other than permeability. Inverse modeling of FFTL is also found useful to identify and estimate initial pressure and initial temperature, which are not properties of the fracture rock but have notable influence on FFTL response.

We have provided the theoretical background necessary to interpret and analyze the pressure and temperature response of FFTL in unsaturated fractured rock. We have illustrated how these data can be used for estimation of transport properties of unsaturated fractured rock. We have also shown (in Paper I) how FFTL data can be utilized to locate the presence of discrete, high-permeability fractures. We are convinced that FFTL has strong potential as a tool for determining location of flowing fractures and

transport properties of fractured rocks. Additionally, while permeability of fractured rock can be estimated using single- and cross-hole pneumatic injection tests [*Guzman et al.*, 1996; *Illman and Neuman*, 2000; *Illman and Neuman*, 2001; *Illman and Neuman*, 2003; *Illman and Tartakovsky*, 2005a,b], the strength of FFTL lies in the fact that it can be used to determine multiple transport properties (e.g., permeability, porosity, and thermal conductivity) from a single experiment.

The usefulness of FFTL can be further improved by improving the logistics (i.e., of not having to manually move the tool from location to location) of logging through implementation of distributed temperature sensor (DTS) technology [see *Selker et al.* 2006, and references therein]. Implementation of DTS, with its enhanced measurement precision, will also increase the utility of FFTL in parameter estimation, because fracture heterogeneities at a smaller scale (i.e., compared to what can be achieved through conventional FFTL) may then be captured as well.

Notation

$1/\alpha$	capillary strength parameter, Pa
C_R	specific heat capacity of rock, J kg^{-1} K^{-1}
C_V	specific heat capacity of air under constant volume, J kg^{-1} K^{-1}
$\mathbf{C_{zz}}$	$m \times m$ *a priori* covariance matrix of measurement error
F^{κ}	Flux of phase κ, kg m^{-2} s^{-1} for $\kappa = 1$ or 2, J m^{-2} s^{-1} for $\kappa = 3$
f_{vpl}	vapor pressure lowering factor
ϕ	porosity
g	acceleration due to gravity, m s^{-2}
Γ_n	surface area of the grid subdomain n, m^2
h_β	specific enthalpy of phase β, J kg^{-1}
k	absolute paermeability, m^2
k_{rg}	gas-phase relative permeability
k_{rl}	liquid-phase relative permeability
λ	van Genuchten exponent
M_w	molecular weight of water, kg mol^{-1}
M^{κ}	Mass or energy accumulation per unit volume for component κ, kg m^{-3} if $\kappa = 1$ or 2, J m-^{3} if $\kappa = 3$.
μ_β	viscosity of phase β, kg m^{-1} s^{-1}
$\mathbf{n}$	unit vector normal to surface Γ_n
P	reference gas phase pressure, Pa
P_β	pressure of phase β, Pa
P_{cl}, $P_{c\beta}$	capillary pressure, Pa

P_{sat}	saturation pressure, Pa
$\mathbf{p}$	parameter vector (dimension n)
q^{κ}	source or sink term for component κ, kg m^{-3} s^{-1} for $\kappa = 1$ or 2, J m^{-3} s^{-1} for $\kappa = 3$
R	universal gas constant, J mol^{-1} K^{-1}
ρ_a	density of air, kg m^{-3}
ρ_β	density of phase β, kg m^{-3}
ρ_R	density of rock formation, kg m^{-3}
$\mathbf{r}$	residual vector (dimension m) with elements $r_i = z_i^* - z_i(\mathbf{p})$
σ_i^2	a priori error variance
s_0^2	a posteriori or estimated error variance
S	objective function, i.e., sum of squared weighted residuals
S_β	saturation of phase β
S^*	reduced liquid saturation
S_{lr}	irreducible liquid saturation
$S_{l,eff}$	effective liquid saturation
T	temperature, ^{o}C
u_β	specific internal energy of phase β, J kg^{-1}
V_n	volume of the grid subdomain n, m^3
$\mathbf{V}_{zz}^{-1}$	$m \times m$ weighting matrix
X_β^κ	mass fraction of component κ in phase β
$\mathbf{z}$	vector of observable variables (dimension m)
$\mathbf{z}^*$	measurement vector (dimension m)

Acknowledgments

We thank the anonymous reviewers for their careful and critical review of the manuscript. We thank Teamrat Ghezzehei and Dan Hawkes of the Ernest Orlando Lawrence Berkeley National Laboratory (Berkeley Lab) for their constructive review of the draft manuscript. We also thank Chin-Fu Tsang and Paul Cook of the Berkeley Lab for sharing the photographs of the FFTL instrument (Figure 1) and the FFTL data (Figure 2) with us. Diana M. Swantek of the Berkeley Lab prepared the graphics for Figure 3, and her contribution is duly acknowledged. This work was supported by the U.S. Department of Energy. The support is provided to Berkeley Lab through the U.S. Department of Energy Contract No. DE-AC02-05CH11231. The United States Government retains and the publisher, by accepting the article for publication, acknowledges that the United States Government retains a non-exclusive, paid-up,

irrevocable, world-wide license to publish or reproduce the published form of this manuscript, or allow others to do so, for United States Government purposes. The views expressed in this article are those of the authors and do not necessarily reflect the views or policies of the United States Department of Energy or the Berkeley Lab.

References

Ahlers, C.F., S. Finsterle, and G.S. Bodvarsson (1999), Characterization of subsurface pneumatic response at Yucca Mountain, Journal of Contaminant Hydrology, 38(1-3), 47-68.

Beven, K. (2006), A manifesto for the equifinality thesis, *Hydrol. J.*, 320, 18-36

Birkholzer, J.T., and Tsang, Y.W. (2000), Modeling the thermal-hydrologic processes in a large-scale underground heater test in partially saturated fractured tuff, *Water Resour. Res.*, 36(6), 1431-1447.

Björnsson, G., A. Hjartarson, G.S. Bodvarsson, and B. Steingrimsson (2003), Development of a 3-D geothermal reservoir model for the greater Hengill volcano in SW-Iceland, In S. Finsterle et al. (eds.), Proceedings of the TOUGH Symposium 2003, LBNL-52494, Lawrence Berkeley Natl. Lab., Berkeley, Calif.

Brodsky, N. S., M. Riggins, J. Connolly, J., and P. Ricci (1997), Thermal expansion, thermal conductivity, and heat capacity measurements for boreholes UE25 NRG-4, UE25 NRG-5, USW NRG-6, and USW NRG-7/7, SAND95-1955 UC-814, Sandia Natl. Lab., Albuquerque, NM.

Brooks, R.H., and J.J. Corey (1964), Hydraulic properties of porous media, *Hydrol. Papers 3*, Colorado State University, Fort Collins, Colorado.

Brutsaert, W. (2005), *Hydrology – An Introduction*, The Cambridge University Press, Cambridge, U.K.

Buesch, D.C. and R.W. Spengler (1998), Character of the middle nonlithophysal zone of the Topopah Spring tuff at Yucca Mountain, Proceedings of the 8th International Conference on High-Level Radioactive Waste Management, American Nuclear Society, April 30-May 2, Las Vegas, NV.

Corey, A.T. (1954), The Interrelation between gas and oil relative permeabilities, *Producers Monthly*, vol. 19, no. 1, pp. 38-41.

Engelhardt, I., S. Finsterle, and C. Hofstee (2003), Experimental and numerical investigation of flow phenomena in nonisothermal, variably saturated bentonite-crushed rock mixtures, *Vadose Zone Journal*, 2, 239-246.

Finsterle, S. (1999a), *i*TOUGH2 User's Guide, LBNL-40040 UC 400, Lawrence Berkeley Natl. Lab., Berkeley, Calif.

Finsterle, S. (1999b), *i*TOUGH2 Command Reference, LBNL-40041 UC 400, Lawrence Berkeley Natl. Lab., Berkeley, Calif.

Finsterle, S (1999c), *i*TOUGH2 Sample Problems, LBNL-40042 UC 400, Lawrence Berkeley Natl. Lab., Berkeley, Calif.

Finsterle, S. (2004), Multiphase inverse modeling: Review and *i*TOUGH2 applications, *Vadose Zone Journal*, 3, 747-762.

Finsterle, S. (2005), Demonstration of optimization techniques for groundwater plume remediation using *i*TOUGH2, *Environmental Modeling and Software*, 21(5), doi:10.1016/j.envsoft.2004.11.012, 665-680.

Finsterle, S. and P. Persoff (1997), Determining permeability of tight rock samples using inverse modeling, *Water Resour. Res.*, 33, 1803-1811.

Finsterle, S. and B. A. Faybishenko (1999), Inverse modeling of a radial multistep outflow experiment for determining unsaturated hydraulic properties, *Advances in Water Resources*, 22(5), 431–444.

Finsterle, S., C. Satik, and M. Guerrero (1998), Analysis of boiling experiments with inverse modeling, p. 281-287, In K. Pruess (ed.) Proceedings of the TOUGH Workshop '98, Rep. LBNL-41995, Lawrence Berkeley Natl. Lab., Berkeley, Calif.

Finsterle, S., K. Pruess, G. Björnsson, and A. Battistelli (2000), Evaluation of geothermal well behavior using inverse modeling, p. 377-387, In B. Faybishenko (ed.) Dynamics of fluids in fractured rocks, Geophys. Monogr., 122, AGU, Washington, DC.

Finsterle, S., C.F. Ahlers, R.C. Trautz, and P.J. Cook (2003), Inverse and predicitive modeling of seepage into underground openings, J. of Contam. Hydrol., 62-63, 89-109.

Freifeld, B.M. (2001), Estimation of fracture porosity of an unsaturated fractured welded tuff using gas tracer testing, Ph.D. Thesis, University of California, Berkeley, Calif.

Ghezzehei, T.A., and H.H. Liu (2004), Calibrated Properties Model, MDL-NBS-HS-000003 REV 02, Bechtel SAIC Company, Las Vegas, NV.

Guzman, A. G., A. M. Geddis, M. J. Henrich, C. F. Lohrstorfer, and S. P. Neuman. (1996), Summary of air permeability data from single-hole injection tests in unsaturated fractured tuffs at the Apache Leap Research Site: Results of steady-state test interpretation, NUREG/CR-6360, U.S. Nuclear Regulatory Commission Washington D.C.

Hirschfelder, J.O., C.F. Curtiss, and R.B. Bird (1954), *Molecular theory of gases and liquids*, John Wiley & Sons, New York, NY.

Huang, K., Y.W. Tsang, and G.S. Bodvarsson (1999), Simultaneous inversion of air-injection tests in fractured unsaturated tuff at Yucca Mountain, *Water Resour. Res.*, 35(8), 2375-2386.

Illman, W. A. (2005), Type curve analyses of pneumatic single-hole tests in unsaturated fractured tuff: Direct evidence for a porosity-scale effect, *Water Resour. Res.*, 41(4), W04018 doi:10.1029/2004WR003703.

Illman W. A. and S. P. Neuman (2000), Type-curve interpretation of multi-rate single-hole pneumatic injection tests in unsaturated fractured rock, *Ground water*, 38(6), 899-911.

Illman, W. A. and S. P. Neuman (2001), Type-curve interpretation of a cross-hole pneumatic test in unsaturated fractured tuff, *Water Resources Research*, 37(3), 583-604.

Illman, W. A. and S. P. Neuman (2003), Steady-state analyses of cross-hole pneumatic injection tests in unsaturated fractured tuff, *Journal of Hydrology*, 281(1-2), 36-54.

Illman, W. A. and D. M. Tartakovsky (2005a), Asymptotic analysis of three-dimensional pressure interference tests: point source solution, *Water Resour. Res.*, 41(1), W01002, doi:10.1029/2004WR003431.

Illman, W. A. and D. M. Tartakovsky (2005b), Asymptotic analysis of cross-hole pneumatic injection tests in unsaturated fractured tuff, *Advances in Water Resources*, 28(11), 1217-1229.

International Formulation Committee (1967), *A formulation of the thermodynamic properties of ordinary water substance*, IFC Secretariat, Düsseldorf, Germany.

Lenhard, R.J., J.C. Parker, and S. Mishra (1989), On the correspondence between Brooks-Corey and van Genuchten models, *Journal of Irrigation and Drainage Engineering-ASCE*, 115, 744.

Levenberg, K. (1944), A method for the solution of certain nonlinear problem in least squares, Quart. Appl. Math., 2, 164-168.

Liu, H.H., C. Doughty, and G.S. Bodvarsson (1998), An active fracture model for unsaturated flow and transport in fracture rocks, *Water Resour. Res.* 34(10): 2633-2646.

Loomis, A.G. (1928), Solubilities of gases in water, in: *International Critical Tables, Vol. III*, E.W. Washburn (ed.), pp. 255-257, McGraw-Hill, New York, NY.

McLaughlin, D. and L.R. Townley (1996), A reassessment of the groundwater inverse problem, *Water Resour. Res*., 32(5), 1131-1161.

Marquardt, D. W. (1963), An algorithm for least squares estimation of nonlinear parameters, *SIAM J. Appl. Math*., 11, 431-441.

Moreno, L. and C.F. Tsang (1991), Multiple-peak response to tracer injection tests in single fractures: a numerical study, *Water Resour. Res*., 27(8), 2143-2150.

Mualem, Y. (1976), A new model for predicting the hydraulic conductivity of unsaturated porous media,*Water Resour. Res*., Vol. 12, No. 3, pp. 513 - 522.

Mukhopadhyay, S. and Y.W. Tsang (2003), Uncertainties in coupled thermal-hydrological processes associated with the Drift Scale Test at Yucca Mountain, Nevada, J. of Contam. Hydrol., 62-63, 595-612.

Mukhopadhyay, S. and Y.W. Tsang (2008), Determination of transport properties from flowing fluid temperature logging in unsaturated fractured rocks: Theory and semi-analytical solution, *Water Resour. Res*., 44, W10424, doi: 10.1029/2008WR006860.

Mukhopadhyay, S., Y.W. Tsang, and J.T. Birkholzer (2007), Estimation of field-scale thermal conductivities of unsaturated fractured rocks from in situ temperature data, *Water Resources Research*, 43, W09418, doi: 10.1029/2006WR005283.

Narasimhan, T.N. and P.A. Witherspoon (1976), An integrated finite difference method for analyzing fluid flow in porous media, *Water Resour. Res.*, 12(1), 57 – 64.

Pruess, K. (1991), TOUGH2—A General-Purpose Numerical Simulator for Multiphase Fluid and Heat Flow, LBNL-29400, Lawrence Berkeley Natl. Lab., Berkeley, Calif.

Pruess, K. and T.N. Narasimhan (1985), A practical method for modeling fluid and heat flow in fractured porous media, *Soc. Pet. Eng. J.*, 25(1), 14 - 26.

Pruess, K., C.M. Oldenburg, and G.J. Moridis (1999), TOUGH2 User's Guide, Version 2.0, LBNL-43134, Lawrence Berkeley Natl. Lab., Berkeley, Calif.

Ramsey, J., J. Bean, C. Lum, and E. Hardin (2004), Thermal Conductivity of the Potential Repository Horizon, MDL-NBS-GS-000005 REV010, Bechtel SAIC Company, Las Vegas, Nevada.

Selker, J.S., L. Thévenaz, H. Huwald, A. Mallet, W. Luxemburg, N. van de Giesen, M. Stejskal, J. Zeman, M. Westhoff, and M.B. Parlange (2006), Distributed fiber-optic temperature sensing for hydrologic systems, *Water Resour. Res*., 42, W12202, doi: 10.1029/2006WR005326.

Tsang, C.F., J. Clyde, P.J. Cook, and R. Solbau (2007), Flowing fluid temperature logging method for determining hydrologic properties of unsaturated fractured rocks, LBNL-63564, Lawrence Berkeley Natl. Lab., Berkeley, Calif.

Tsang, Y.W. and J.T. Birkholzer (1999), Predictions and observations of the thermal-hydrological conditions in the Single Heater Test, J. of Contam. Hydrol., 38(1), 385-425.

Unger, A., S. Finsterle, and G.S. Bodvarsson (2004), Transport of radon gas into a tunnel at Yucca Mountain – Estimating large-scale fractured tuff hydraulic properties and implications for operation of the ventilation system, *J. of Contam. Hydrol.*, 70, 153-171.

van Genuchten, M.Th. (1980), A closed-form equation for predicting the hydraulic conductivity of unsaturated soils, *Soil Sci. Soc*., 44, 892-898.

White, S., A. Creighton, P. Bixley, and W. Kissling (2003), Modeling the dewatering and depressurization of the Lihir open pit gold mine, In S. Finsterle et al. (eds.) Proceedings of the TOUGH Symposium 2003, LBNL-52494, Lawrence Berkeley Natl. Lab., Berkeley, Calif.

Zarrouk, S., M. O'Sullivan, A. Croucher, and W. Mannington (2007), Numerical modelling of production from the Poihipi dry steam zone: Wairakei geothermal system, New Zealand, *Geothermics*, 36, 289-303.

Zimmermann, D.A., G. de Marsily, C.A. Gotway, M.G. Marietta, C.L. Axness, R.L. Beauheim, R.L. Bras, J. Carrera, G. Dagan, P.B. Davies, D.P. Gallegos, A. Galli, J. Gomez-Hernandez, P. Grindrod, A.L. Gutjhar, P.K. Kitanidis, A.M. Lavenue, D. McLaughlin, S.P. Neuman, B.S. Rama Rao, C. Ravenne, and Y. Rubin (1998), A comparison of seven geostatistically based inverse approaches to estimate transmissivities for modeling advective transport by groundwater flow, *Water Resour. Res.*, 34, 1373-1413.

Appendix A

The basic mass- and energy-balance equations solved by TOUGH2 [*Pruess*, 1991; *Pruess et al*., 1999] can be written in the general form

$$\frac{d}{dt}\int_{V_n} M^{\kappa}\, dV_n = \int_{\Gamma_n} \boldsymbol{F}^{\kappa}\boldsymbol{n}\; d\Gamma_n + \int_{V_n} q^{\kappa}\, dV_n \tag{A.1}$$

The integration is over an arbitrary subdomain V_n, which is bounded by the closed surface Γ_n. The quantity M appearing in the accumulation term on the left hand side of Equation A.1 represents mass or energy per volume, with κ = 1, 2 labeling the mass components water and air, and κ = 3 the "heat component." F denotes mass or heat flux (see below), q denotes sinks and sources, and n is a normal vector on surface element $d\Gamma_n$, pointing inward into V_n.

The general form of the mass accumulation term is

$$M^{\kappa} = \phi \sum_{\beta} S_{\beta}\rho_{\beta}X_{\beta}^{\kappa} \tag{A.2}$$

The total mass of component κ is obtained by summing over the phases β (= liquid, gas), with ϕ the porosity, S_β the saturation of phase β (i.e., the fraction of pore volume occupied by phase β), ρ_β the density of phase β, and X_{β}^{κ} the mass fraction of component κ in phase β. Similarly, the heat accumulation term in a multiphase system is

$$\boldsymbol{M}^{3} = (1-\phi)\rho_{\boldsymbol{R}}\boldsymbol{C}_{\boldsymbol{R}}\boldsymbol{T} + \phi\sum_{\beta}\boldsymbol{S}_{\beta}\rho_{\beta}\boldsymbol{u}_{\beta} \tag{A.3}$$

where ρ_R and C_R are, respectively, rock-grain density and specific heat capacity of the rock, T is temperature, and u_β is specific internal energy in phase β.

Advective mass flux is a sum over phases,

$$\boldsymbol{F}^{\kappa}\Big|_{adv} = \sum_{\beta} X_{\beta}^{\kappa}\boldsymbol{F}_{\beta}, \tag{A.4}$$

and individual phase fluxes are given by a multiphase version of Darcy's law (continuum representation),

$$\mathbf{F}_\beta = \rho_\beta \mathbf{u}_\beta = -\boldsymbol{k}\frac{\boldsymbol{k}_{r\beta}\rho_\beta}{\mu_\beta}\left(\nabla \boldsymbol{P}_\beta - \rho_\beta \mathbf{g}\right) \tag{A.5}$$

Here, $\mathbf{u}_\beta$ is the Darcy velocity in phase β, k is absolute permeability, $k_{r\beta}$ is the relative permeability to phase β, μ_β is viscosity, and

$$P_\beta = P + P_{c\beta} \tag{A.6}$$

is the fluid pressure in phase β, which is the sum of the pressure P of a reference phase (gas pressure) and the capillary pressure $P_{c\beta}$ (≤ 0); and g is the vector of gravitational acceleration. Vapor-pressure lowering is modeled by Kelvin's equation

$$P_v\left(T, S_l\right) = f_{vpl}(T, S_l)\, P_{sat}(T) \tag{A.7}$$

where

$$f_{vpl} = exp\left[\frac{M_w P_{cl}\left(S_l\right)}{\rho_l R\left(T + 273.15\right)}\right] \tag{A.8}$$

is the vapor-pressure lowering factor, identical to the definition of relative humidity. P_{sat} is the saturated vapor pressure of the bulk liquid phase, P_{cl} is the difference between liquid and gas phase pressure, M_w is the molecular weight of water, and R is the universal gas constant. Vapor pressure lowering is a well known physical process that allows for the presence of liquid water in small rock pores at temperatures above the nominal boiling point.

Heat flux includes conductive and convective components

$$\boldsymbol{F}^3 = -\lambda \nabla T + \sum_\beta h_\beta F_\beta \tag{A.9}$$

where λ is the thermal conductivity of the rock-fluid mixture, and h_β is the specific enthalpy in phase β.

The transport equations given above are complemented with constitutive relationships, which express all parameters as a function of a set of primary variables. In TOUGH2

[*Pruess*, 1991; *Pruess et al*., 1999], the thermophysical properties of water substance are accurately described by the steam table equations, as given by the *International Formulation Committee* [1967]. Air is approximated as an ideal gas, and gas pressure is the sum of the partial pressures for air and vapor. The solubility of air in liquid water is calculated from Henry's law.

Capillary pressures and relative permeabilities depend on phase saturation. For liquid, the capillary suction and the liquid-phase relative permeability have the van Genuchten functional forms [*van Genuchten*, 1980; *Mualem*, 1976]:

$$P_{cl} = -\frac{1}{\alpha}\left[\left(S_{l,eff}\right)^{-1/\lambda} - 1\right]^{1-\lambda}$$

$$k_{rl} = \left(S_{l,eff}\right)^{1/2}\left[1-\left(1-\left(S_{l,eff}\right)^{1/\lambda}\right)^{\lambda}\right]^{2} \qquad \text{(A.10)}$$

$$S_{l,eff} = \frac{\left(S_l - S_{lr}\right)}{\left(1 - S_{lr}\right)}$$

where $S_{l,eff}$ is liquid effective saturation, S_l is liquid saturation, S_{lr} is liquid residual saturation, λ is the van Genuchten exponent, and $1/\alpha$ is the capillary strength of the porous medium. Relative permeability for gas flow is described by the van Genuchten formulations [*van Genuchten*, 1980] formulation as follows:

$$k_{rg} = 1 - k_{rl} \qquad \text{(A.11)}$$

The selected formulations for the dependence of the capillary pressure and the relative permeability on liquid-phase saturation are widely employed in the literature.

In the TOUGH2 simulator [*Pruess 1991*; *Pruess et al*., 1999], the continuum balance equations are discretized in space using the integral finite difference approach, and time is discretized as fully implicit. The discretized balance equations are written in terms of residuals (difference in the primary variables between two successive iteration steps at all space locations) and iteration is continued until the residuals are reduced below a preset convergence tolerance. If convergence cannot be achieved within a certain number of

(default or user supplied) iterations, the time step size is automatically reduced and a new iteration process is started. This ensures adequate time-stepping control without compromising accuracy.

Figure Captions

Figure 1. Photograph of the FFTL instrument (a) the whole logging tool, and (b) close-up view (from *Tsang et al*., 2007).

Figure 2. Sample FFTL data from Borehole 182 of the ESF at Yucca Mountain, Nevada: (a) pressure and pumping data, and (b) temperature data

Figure 3. Schematic representation of the conceptual model for a FFTL experiment

Figure 4. Transient pressure response from forward simulations with different locations of the constant source. Measured pressure data are also included for comparison.

Figure 5. Scaled sensitivity coefficients (see Equation 7) to calculated system response as a function of time for selected parameters, (a) pressure, and (b) temperature

Figure 6. Scaled total sensitivity coefficients for pressure and temperature response for each of the selected parameter, as indicated on the horizontal axis.

Figure 7. Actual and fitted pumping rate as a function of time

Figure 8. Comparison of pressure and temperature response using actual and smoothed pumping rates. Measured pressure and temperature response are also included for comparison.

Figure 9. Complete temperature data from FFTL in Borehole 182 at Yucca Mountain. Temperature data shown in the inset were selected for parameter estimation.

Figure 10. Comparison of measured pressure and temperature response from FFTL with simulated best-fit pressure and temperature response, when only permeability, porosity, and thermal conductivity are subjected to parameter estimation (i.e., initial pressure and temperature are assumed known)

Figure 11. Comparison of measured pressure and temperature response from FFTL with simulated best-fit pressure and temperature response, when permeability, porosity, thermal conductivity, initial pressure, and temperature are subjected to parameter estimation

Table Captions

Table 1. Hydrological and thermal properties of the fracture continuum used in sensitivity studies of Sections 4 and 5

Table 2. Best-fit parameter estimates and statistics of fit when only permeability, porosity, and thermal conductivity are subjected to parameter estimation, i.e., initial pressure and temperature are assumed known (see Figure 10)

Table 3. Best-fit parameter estimates and statistics of fit when permeability, porosity, thermal conductivity, initial pressure, and initial temperature are subjected to parameter estimation (see Figure 11)

Table 4. Comparison of estimated best-fit parameter values (for permeability, porosity, and thermal conductivity) it this paper with previous independent best-fit estimates of the same

Table 1.

Parameter Name	**Value**
Permeability	4.0×10^{-13} m^2
Porosity	0.01
Density	2540 kg m^{-3}
Thermal conductivity	2.0 W m^{-1} K^{-1}
Specific heat capacity	1000 J kg^{-1} K^{-1}
Gas Saturation	98%
Liquid saturation	2%
Residual liquid saturation	1%
van Genuchten α	1×10^{-3} Pa^{-1}
van Genuchten m	0.633

Table 2.

Parameter	Best-fit value	Standard Deviation		Sensitivity	
		σ_p	σ_p^* / σ_p	Output	Objective Function
log(permeability, m^2)	-12.48	2.75×10^{-2}	0.995	34025.8	140.6
log(porosity)	-1.37	0.76×10^{-1}	0.981	198.6	0.300
Thermal conductivity, W m^{-1} K^{-1}	1.47	0.264	0.983	29.4	0.210

Table 3.

Parameter	Best-fit value	Standard Deviation		Sensitivity	
		σ_p	σ_p^* / σ_p	Output	Objective Function
log(permeability, m^2)	-12.48	2.77×10^{-2}	0.541	30924.7	96.950
log(porosity)	-2.04	0.137	0.896	23.2	0.958
Thermal conductivity, $W\ m^{-1}\ K^{-1}$	1.68	0.336	0.904	5.6	0.049
Initial pressure, Pa	85547	83.1	0.541	207.9	4425.024
Initial temperature, ^oC	24.15	0.26×10^{-2}	0.995	897.4	104417.032

Table 4.

Parameter	Estimated best-fit values (in this paper)	Previous estimates	
		Best-fit values	Source and methodology
log(permeability, m^2)	-12.48	-13.00	*Huang et al*. [1999], air-injection testing
		-12.89	*Birkholzer and Tsang* [2000]; *Freifeld* [2001], air-injection testing
log(porosity)	-2.04	-2.52	*Freifeld* [2001], Gas tracer tests
		-2.07	*Ghezzehei and Liu* [2004], air-injection and gas tracer tests

Thermal conductivity, W m^{-1} K^{-1}	1.68	1.67	*Brodsky et al.* [1997], thermal conductivity measurements of cores
		1.42	*Ramsey et al.* [2004], geostatistical simulation using measured thermal conductivity values from cores as input
		1.41	*Mukhopadhyay et al.* [2007], from temperature data collected from the Drift Scale Test at Yucca Mountain

Figure 1a.

Figure 1b.

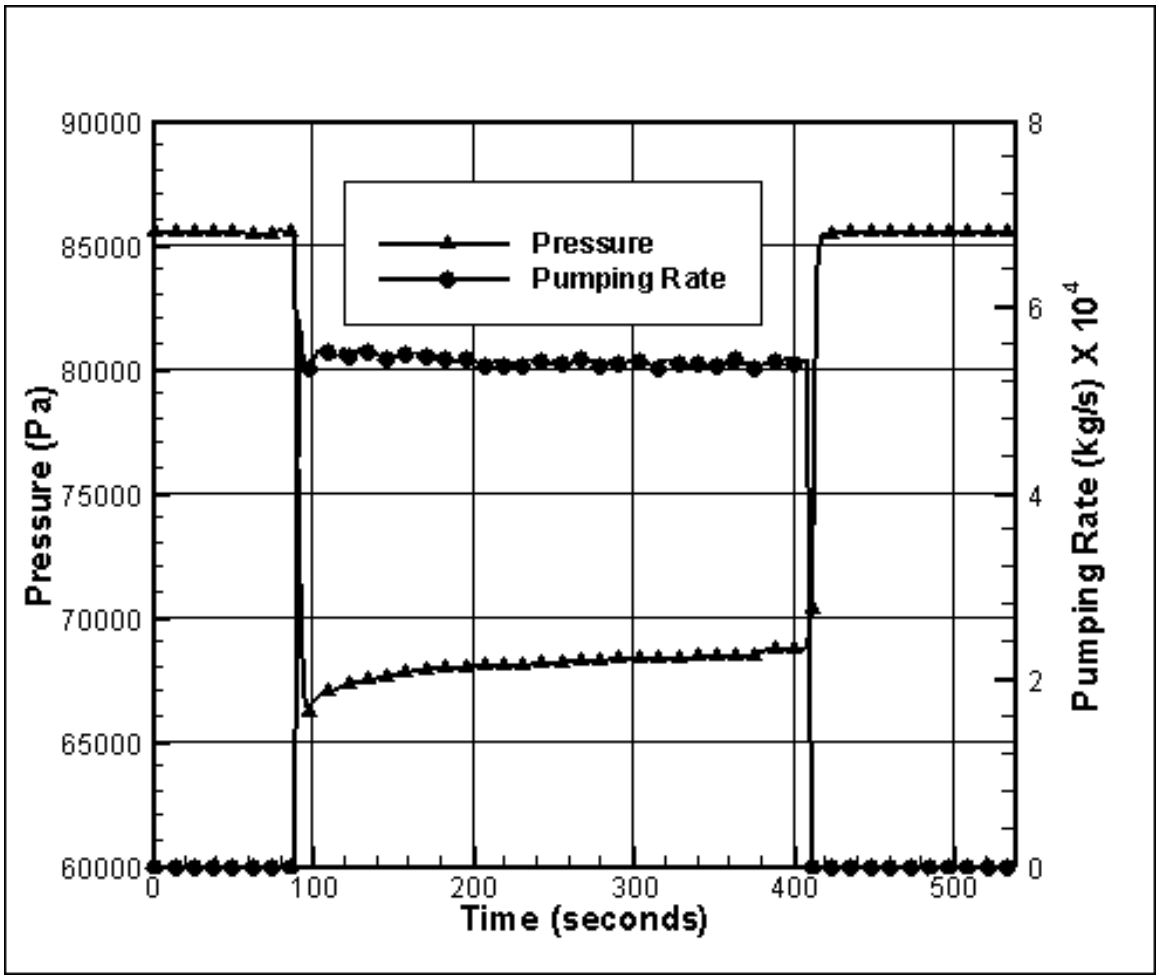
90000
85000
80000
75000
70000
65000
60000
Pressure (Pa)
8
6
4
2
0
Pumping Rate (kg/s) X 10^4
0
100
200
300
400
500
Time (seconds)
Pressure
Pumping Rate
Figure 2a.

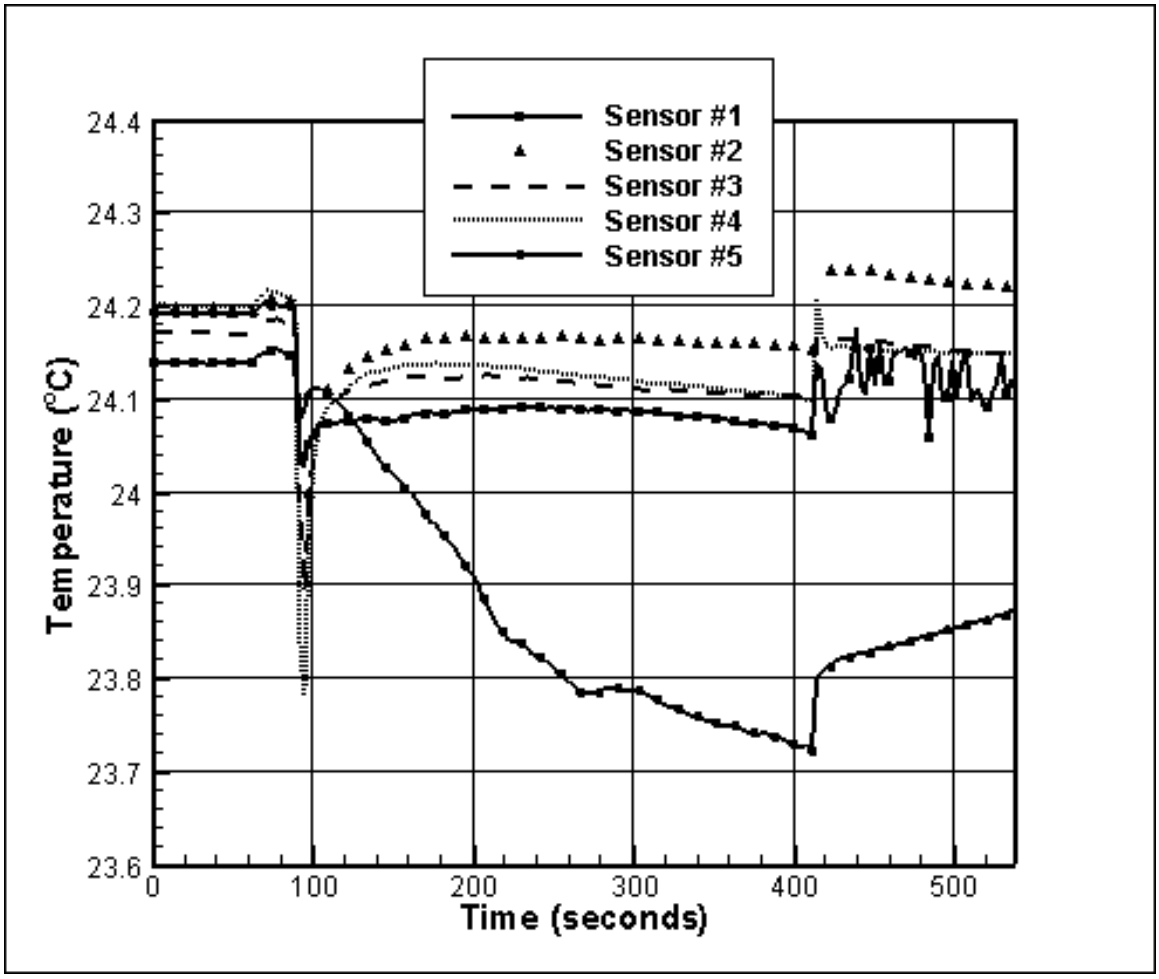
Sensor #1
Sensor #2
Sensor #3
Sensor #4
Sensor #5
24.4
24.3
24.2
24.1
24
23.9
23.8
23.7
23.6
Temperature (°C)
0
100
200
300
400
500
Time (seconds)
Figure 2b.

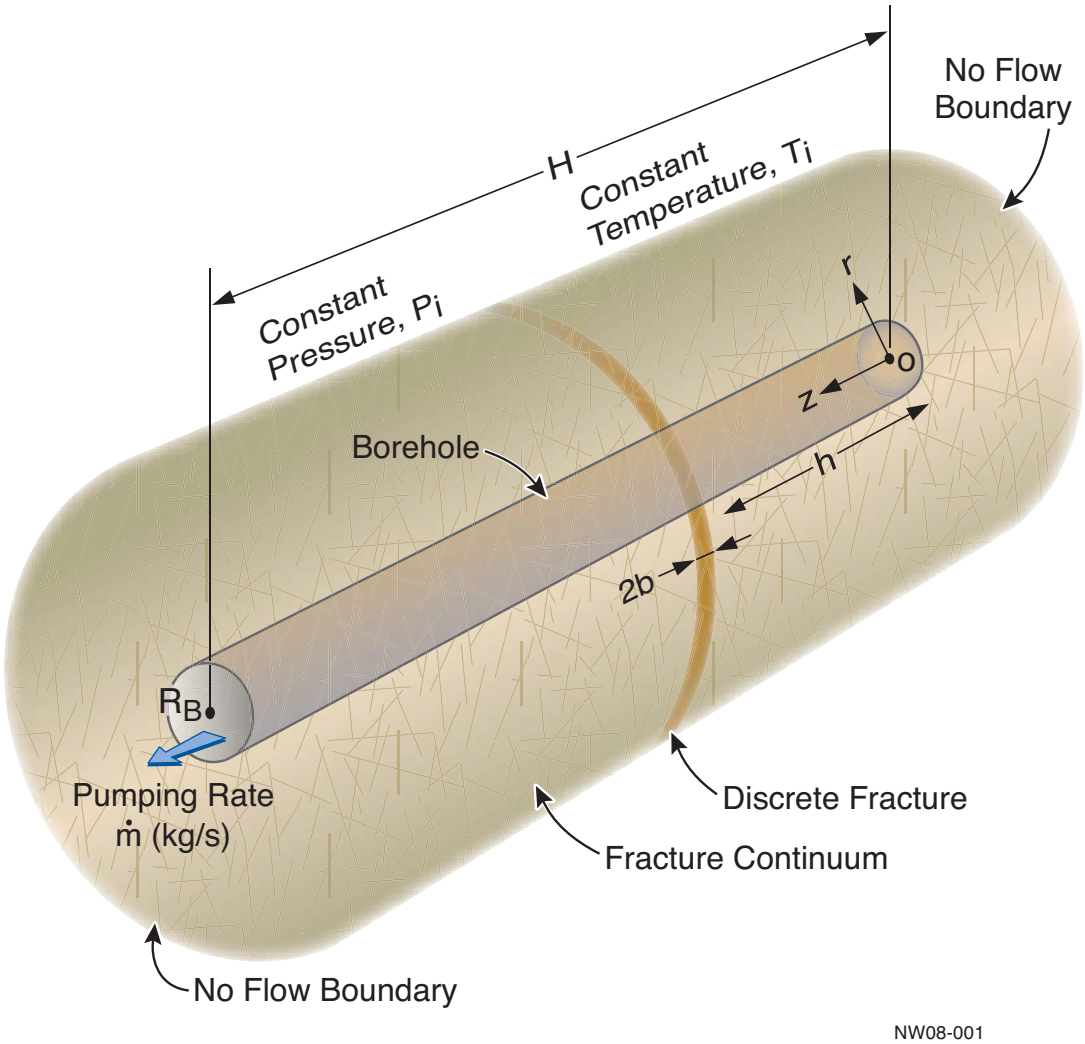
No Flow
Boundary
H
Constant
Temperature, Ti
Constant
Pressure, Pi
r
o
z
Borehole
h
2b
RB
Pumping Rate
ṁ (kg/s)
Discrete Fracture
Fracture Continuum
No Flow Boundary
NW08-001

Figure 3.

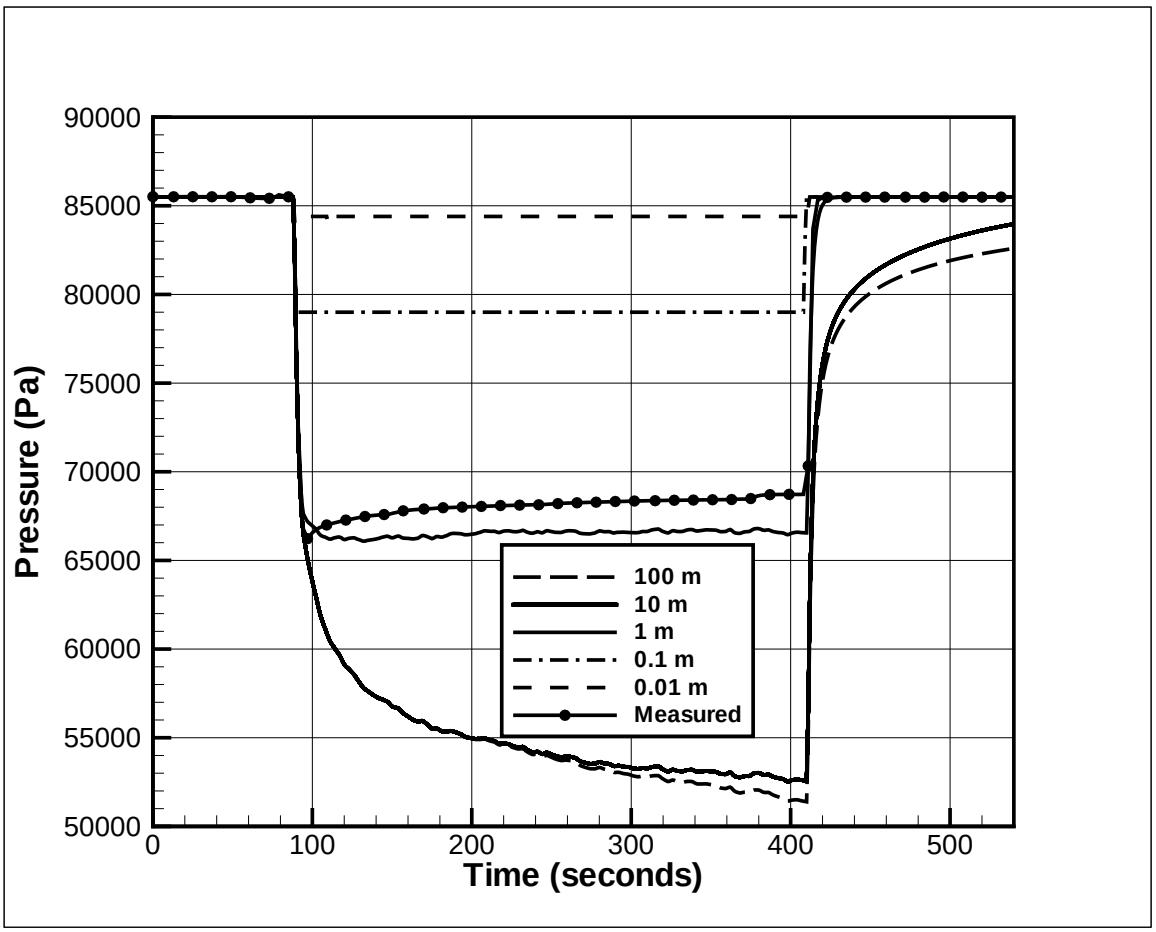
90000
85000
80000
75000
70000
65000
60000
55000
50000
Pressure (Pa)
0
100
200
300
400
500
Time (seconds)
100 m
10 m
1 m
0.1 m
0.01 m
Measured
Figure 4.

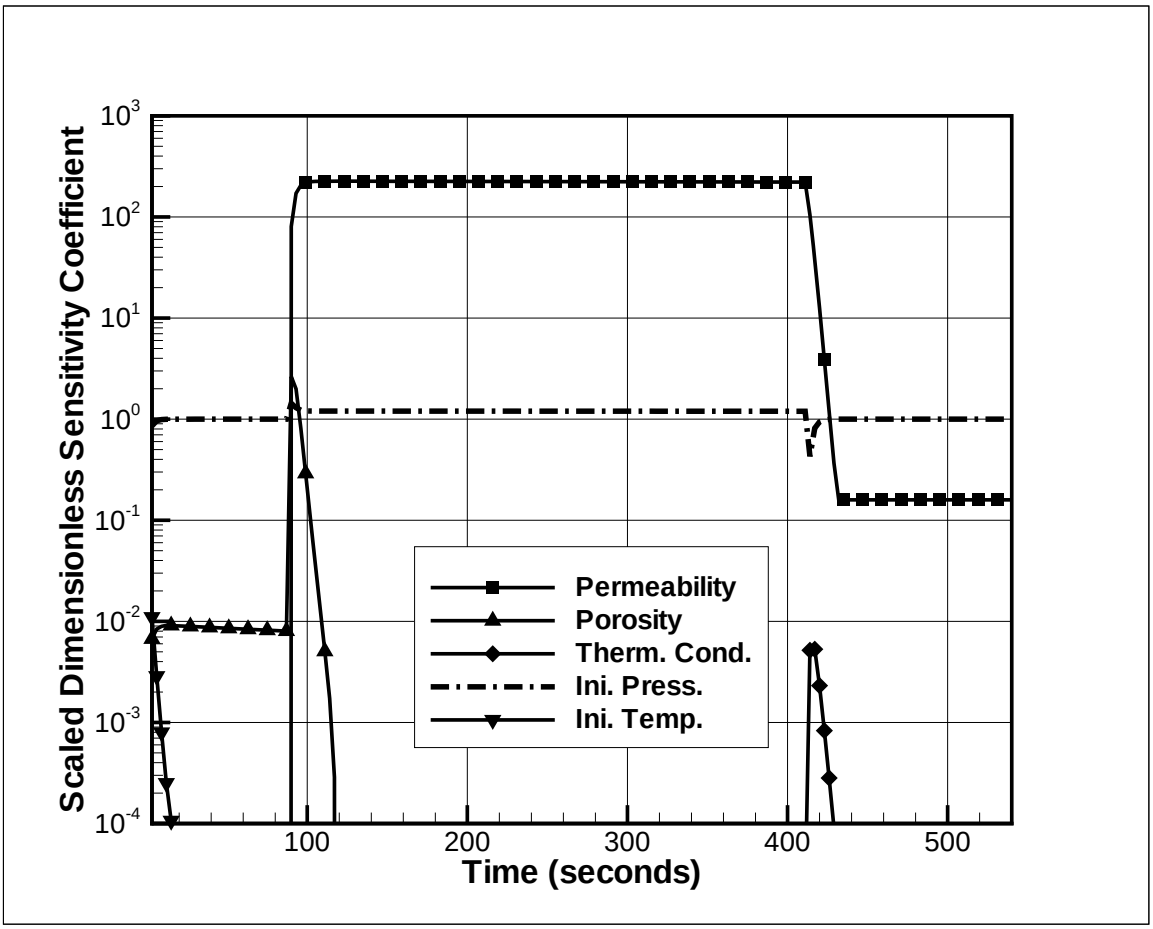
Scaled Dimensionless Sensitivity Coefficient
10^3
10^2
10^1
10^0
10^-1
10^-2
10^-3
10^-4
100
200
300
400
500
Time (seconds)
Permeability
Porosity
Therm. Cond.
Ini. Press.
Ini. Temp.

Figure 5a.

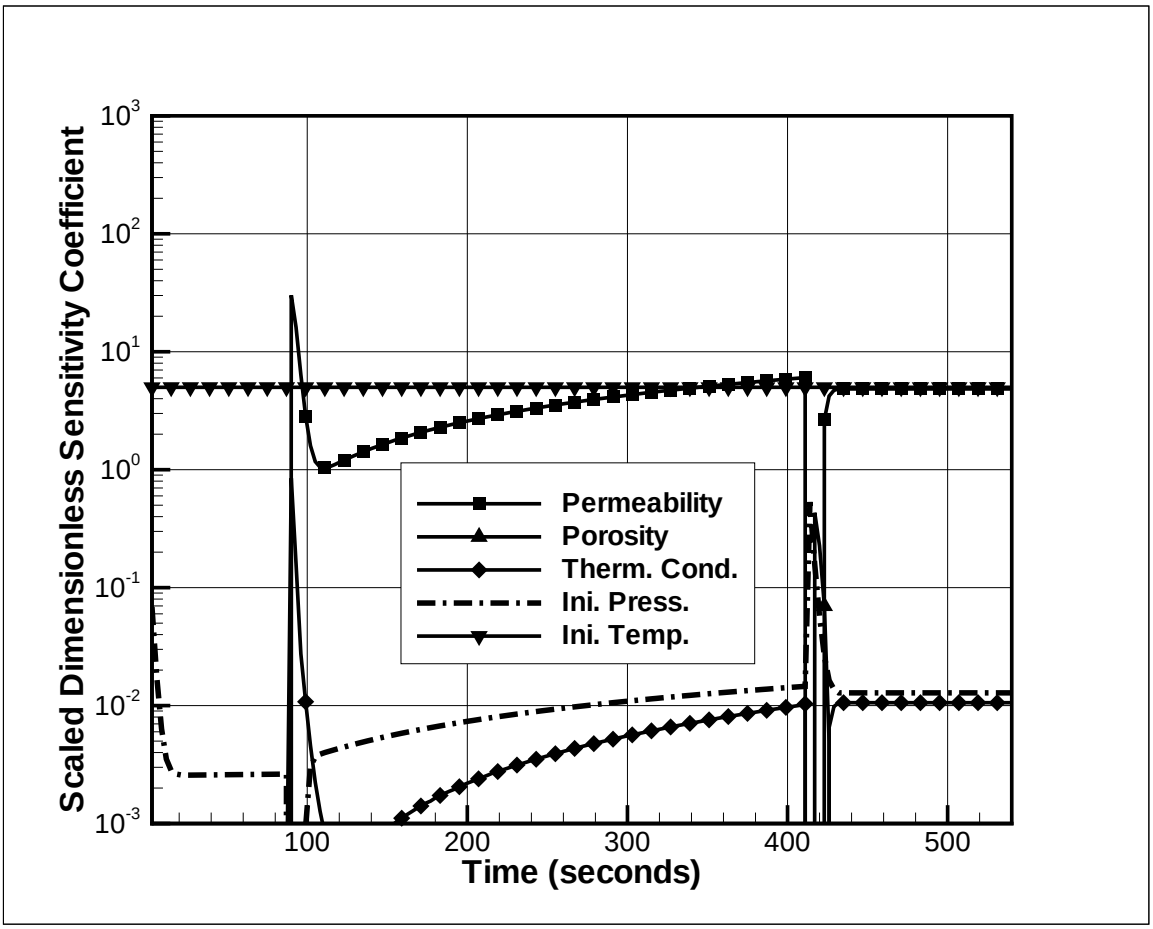
Scaled Dimensionless Sensitivity Coefficient
10^3
10^2
10^1
10^0
10^-1
10^-2
10^-3
100
200
300
400
500
Time (seconds)
Permeability
Porosity
Therm. Cond.
Ini. Press.
Ini. Temp.

Figure 5b.

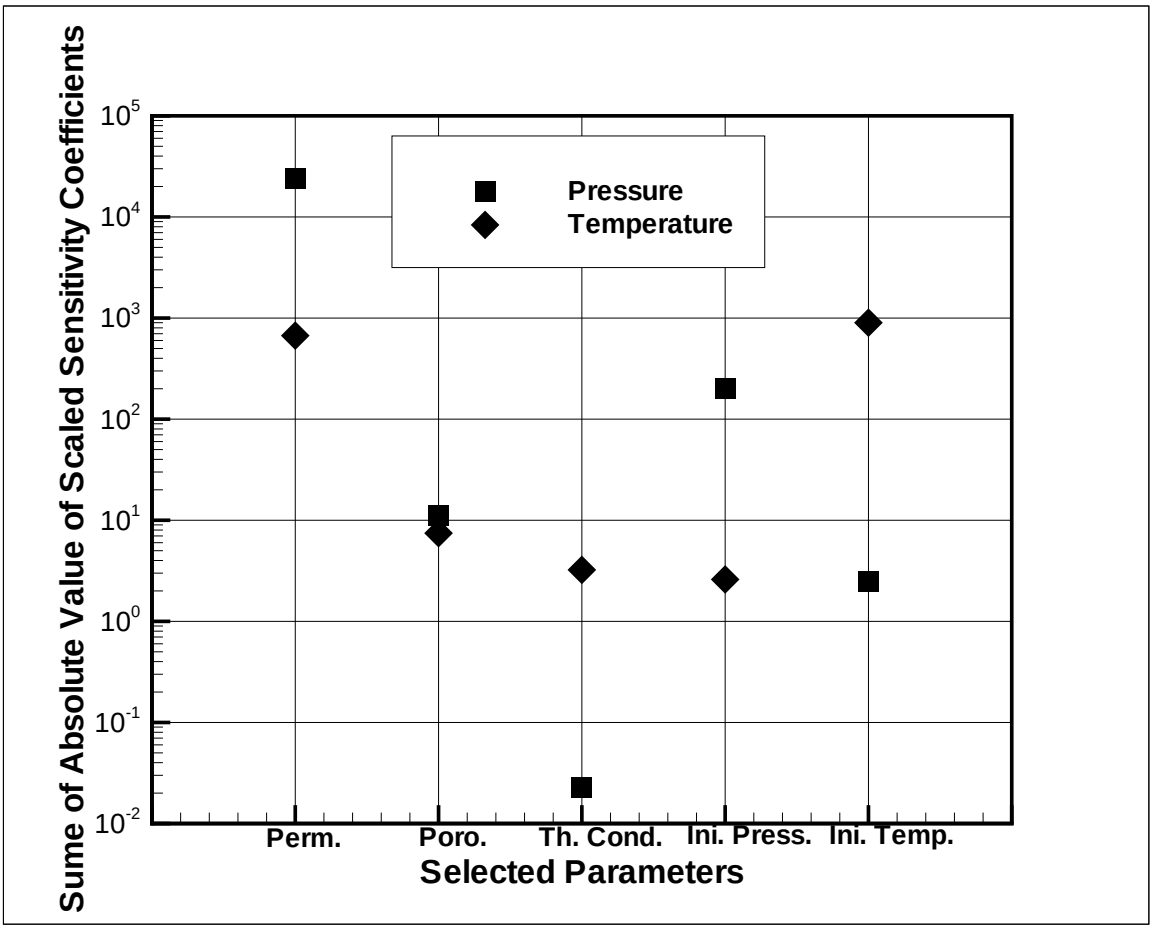
Sume of Absolute Value of Scaled Sensitivity Coefficients
10^5
10^4
10^3
10^2
10^1
10^0
10^-1
10^-2
Pressure
Temperature
Perm.
Poro.
Th. Cond.
Ini. Press.
Ini. Temp.
Selected Parameters

Figure 6.

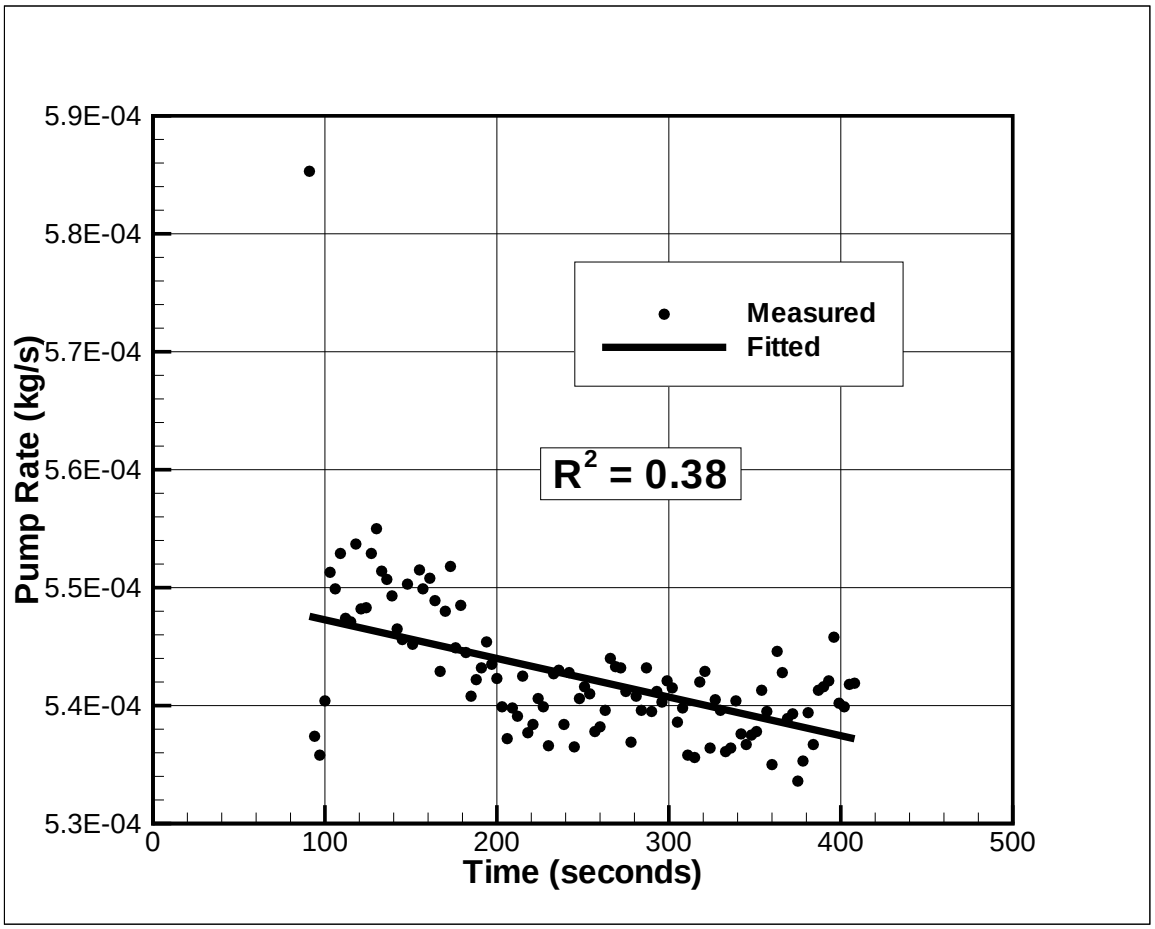
5.9E-04
5.8E-04
5.7E-04
5.6E-04
5.5E-04
5.4E-04
5.3E-04
Pump Rate (kg/s)
0
100
200
300
400
500
Time (seconds)
Measured
Fitted
R2 = 0.38

Figure 7

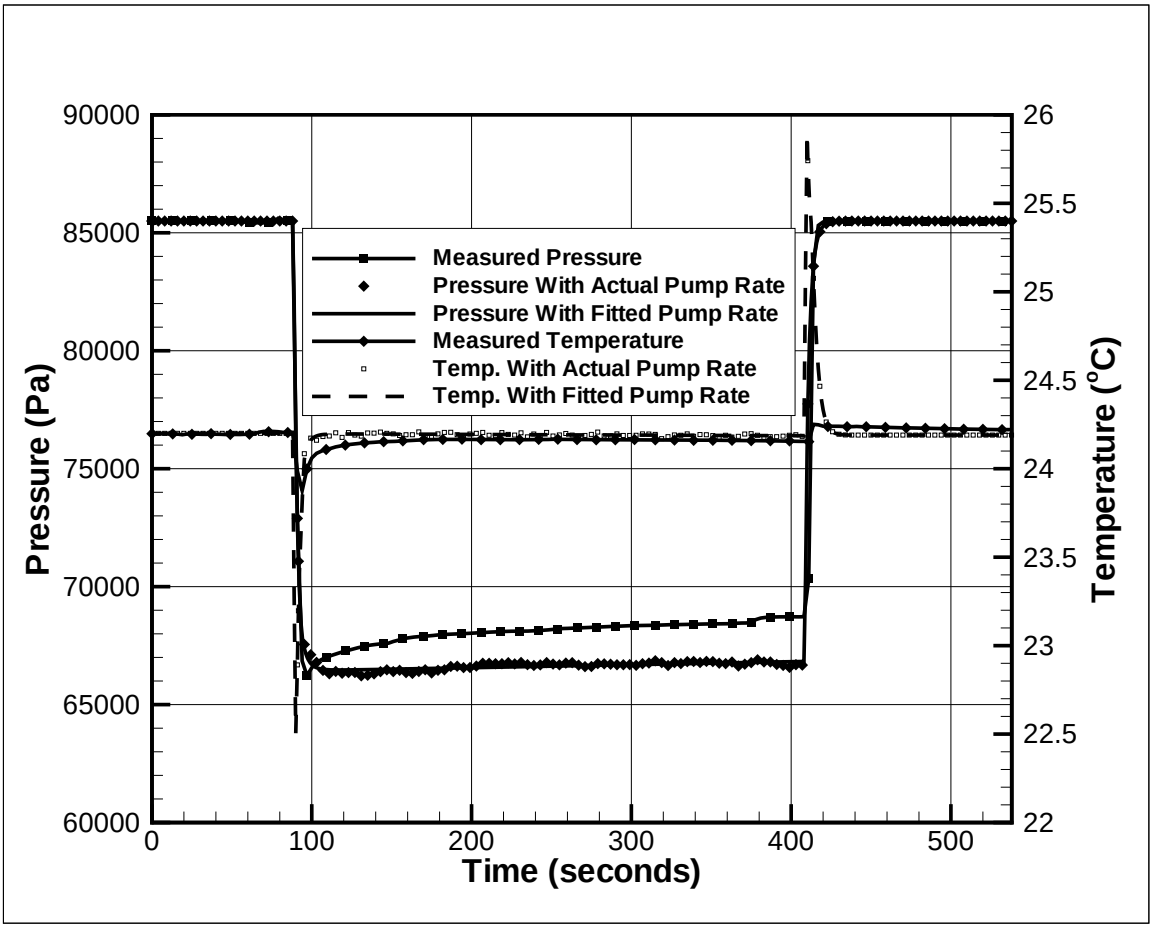
90000
85000
80000
75000
70000
65000
60000
Pressure (Pa)
26
25.5
25
24.5
24
23.5
23
22.5
22
Temperature (°C)
0
100
200
300
400
500
Time (seconds)
Measured Pressure
Pressure With Actual Pump Rate
Pressure With Fitted Pump Rate
Measured Temperature
Temp. With Actual Pump Rate
Temp. With Fitted Pump Rate

Figure 8.

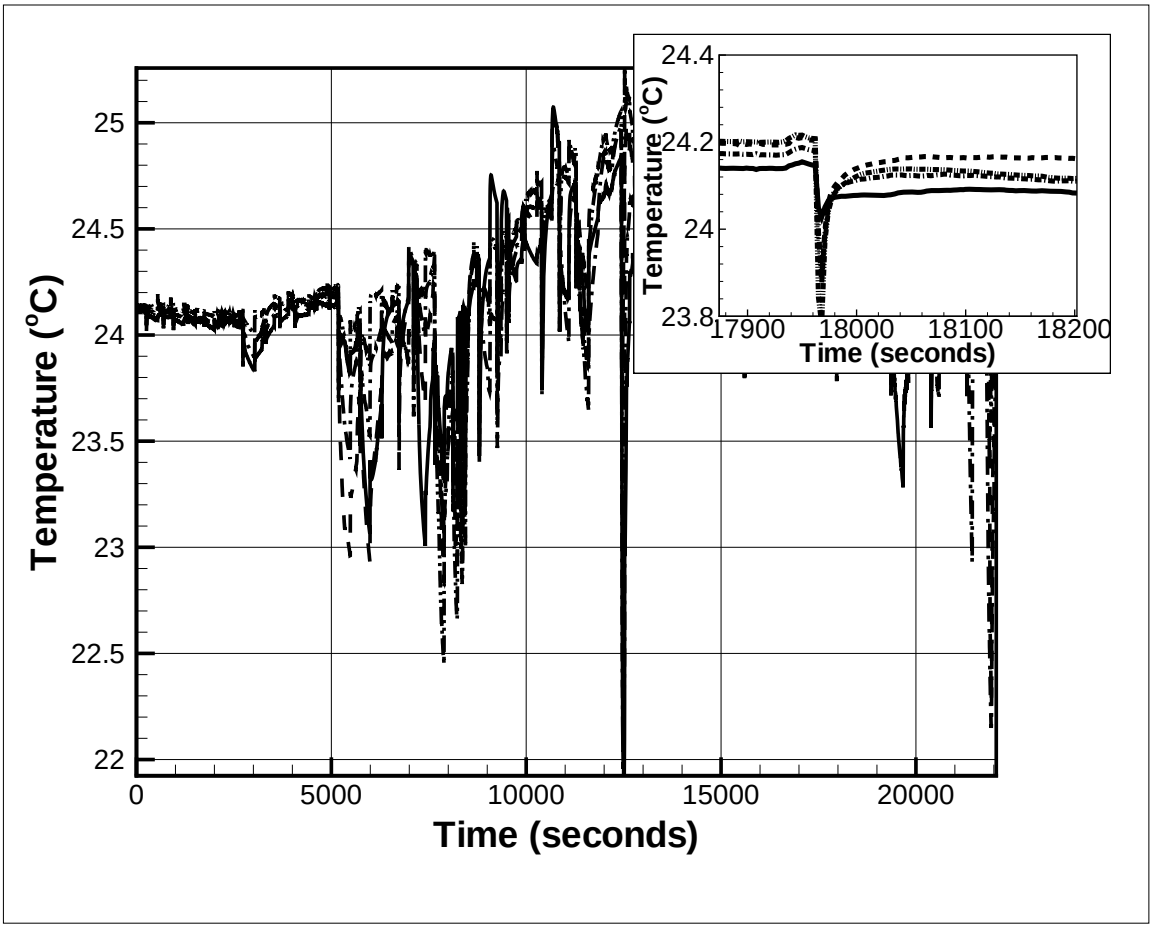
Temperature (°C)
25
24.5
24
23.5
23
22.5
22
0
5000
10000
15000
20000
Time (seconds)
Temperature (°C)
24.4
24.2
24
23.8
17900
18000
18100
18200
Time (seconds)

Figure 9.

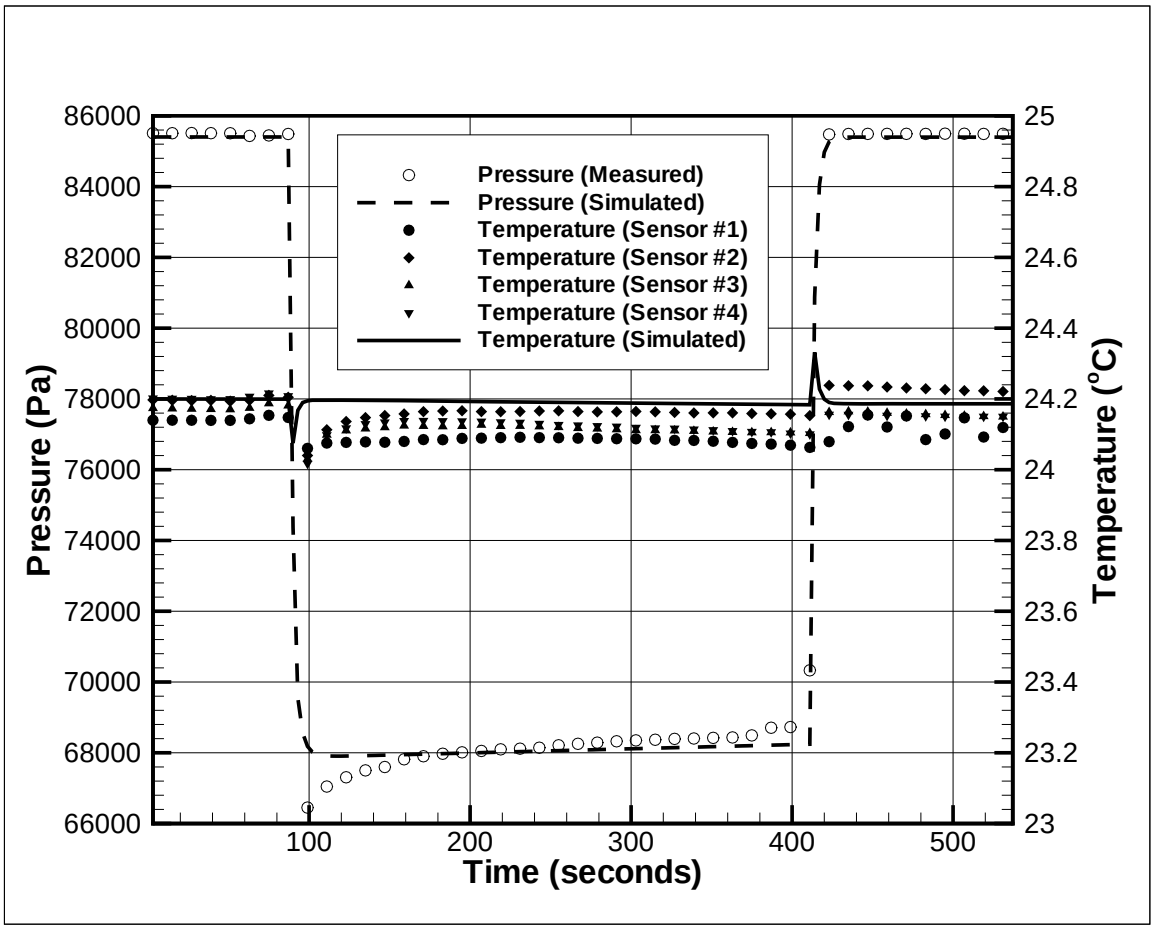
Pressure (Measured)
Pressure (Simulated)
Temperature (Sensor #1)
Temperature (Sensor #2)
Temperature (Sensor #3)
Temperature (Sensor #4)
Temperature (Simulated)
Pressure (Pa)
Temperature (°C)
Time (seconds)
86000
84000
82000
80000
78000
76000
74000
72000
70000
68000
66000
25
24.8
24.6
24.4
24.2
24
23.8
23.6
23.4
23.2
23
100
200
300
400
500

Figure 10.

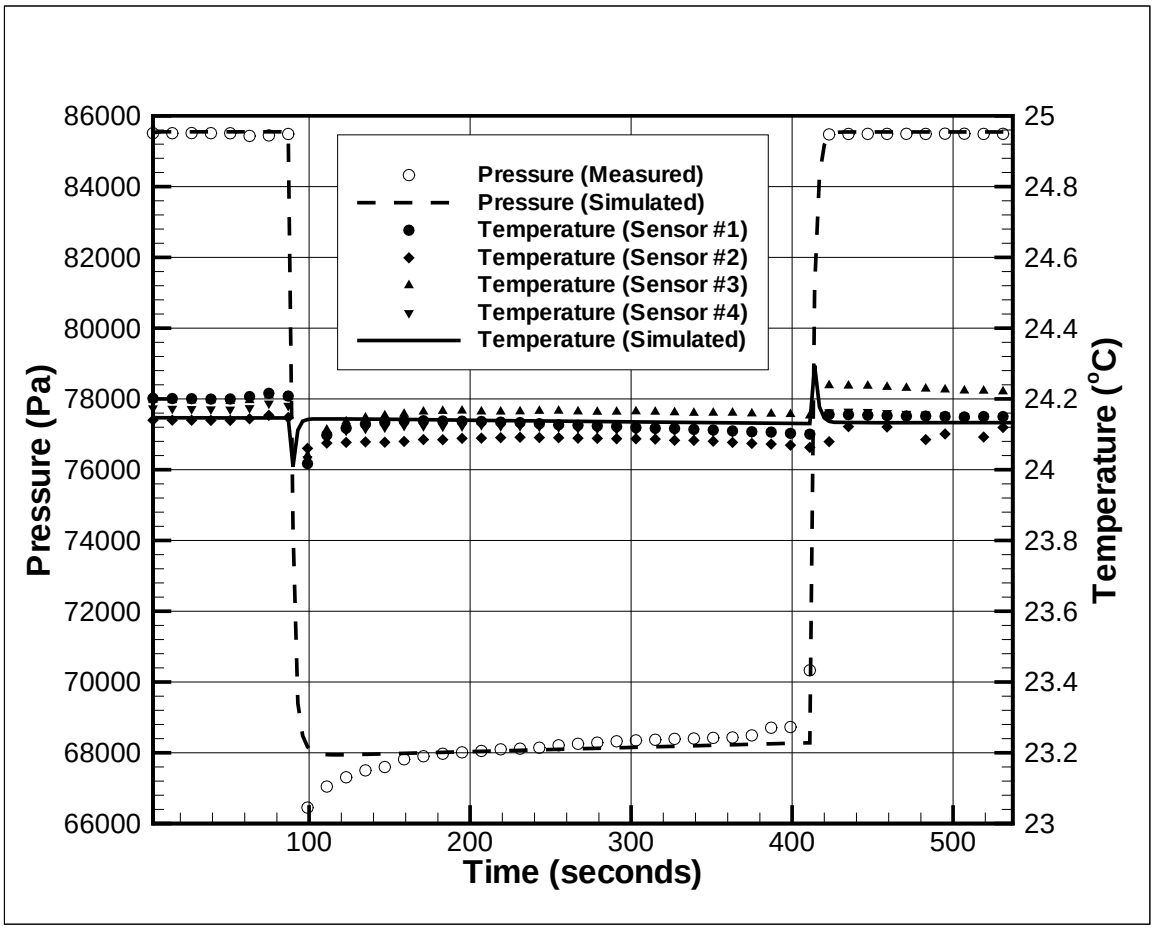
Pressure (Measured)
Pressure (Simulated)
Temperature (Sensor #1)
Temperature (Sensor #2)
Temperature (Sensor #3)
Temperature (Sensor #4)
Temperature (Simulated)
Pressure (Pa)
Temperature (°C)
Time (seconds)
86000
84000
82000
80000
78000
76000
74000
72000
70000
68000
66000
25
24.8
24.6
24.4
24.2
24
23.8
23.6
23.4
23.2
23
100
200
300
400
500

Figure 11.